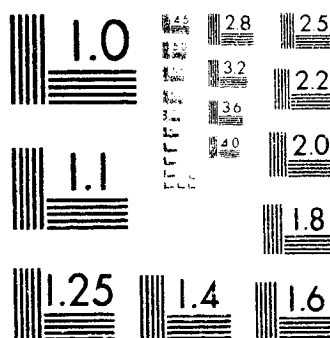


1 OF 1

N 79 18286

UNCLAS



MICROCOPY RESOLUTION TEST CHART
NATIONAL BUREAU OF STANDARDS-1963-A

NASA CR-144878

A WATER TUNNEL FLOW VISUALIZATION

STUDY OF THE F-15

(NASA-CR-144878) A WATER TUNNEL FLOW
VISUALIZATION STUDY OF THE F-15 Final
Report (Northrop Corporate Labs.) 96 p
HC A05/MF A01

N79-18286

CSCI 20D

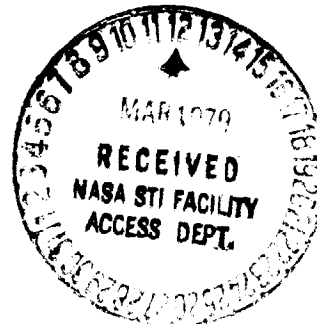
G3/34

Unclas
14678

Dale J. Lorincz

Northrop Corporation
Aircraft Group
Hawthorne, California 90250

December 1978



Prepared for

NATIONAL AERONAUTICS AND SPACE ADMINISTRATION
Dryden Flight Research Center
Edwards, California 93523

FOREWORD

This report documents the results of a detailed study of the vortex flow of the F-15 wing and forebody. The effect on the wing flow field of angle of attack and sideslip, inlet mass flow rate, and inlet bow deflection were investigated. In addition to the production forebody, forebodies with different fineness ratios and cross-sectional shapes were tested with and without a noseboom. The flow visualization work was performed in the Northrop diagnostic water tunnel. The author wishes to thank Mr. Edward L. Friend of NASA Dryden Flight Research Center for his assistance during the water tunnel testing and his support throughout this study.

This report was prepared by the Northrop Corporation under NASA contract NAS4-2526. The contract work was performed during the period May 1978 to September 1978.

CONTENTS

SUMMARY	1
INTRODUCTION	2
SYMBOLS	4
TEST FACILITY AND PROCEDURE	5
Water Tunnel Facility	5
Test Procedure	5
Past Water Tunnel Results	6
Delta Wings	6
Tangent Ogives	7
MODEL DESCRIPTION	7
RESULTS AND DISCUSSION	8
Wing Flow Field Characteristics	9
Full-Scale Tuft Study	11
Inlet Mass Flow Effects	14
Sideslip Effects	16
Inlet Cowl Deflection Angle	20
Forebody Fineness Ratio Effects	21
Production Forebody	21
Long Forebody	25
Forebody Cross-Sectional Shape	28
Cambered Forebody	28

CONTENTS (Continued)

Nose Boom Effects	30
Production Forebody	30
Long Forebody	32
Cambered Forebody	33
Helical Separation Trip	34
Wing-Fuselage Underside Vortex	36
CONCLUSIONS	37
REFERENCES	40

A WATER TUNNEL FLOW
VISUALIZATION STUDY OF THE F-15

By Dale J. Lorincz
Northrop Corporation, Aircraft Group
Hawthorne, California

SUMMARY

Water tunnel studies have been performed to qualitatively define the flow field of the F-15 aircraft. Particular emphasis was placed on defining vortex flows generated at high angles of attack. The flow visualization tests were conducted in the Northrop diagnostic water tunnel using a 1/48-scale model of the F-15. Flow visualization pictures were obtained over an angle-of-attack range to 55° and sideslip angles up to 10° .

The basic aircraft configuration was investigated in detail to determine the vortex flow field development, vortex path, and vortex breakdown characteristics as a function of angle of attack and sideslip. The mapping of this flow field was done to assist NASA DFRC in planning future studies on the full-scale aircraft or the remotely piloted 3/8-scale model. The vortex flow patterns observed in the water tunnel were found to aid in understanding the results of a tuft study performed by NASA DFRC of the full-scale aircraft in flight.

Additional tests were performed to determine the sensitivity of the wing upper surface vortex flow fields to variations in inlet mass flow ratio and inlet cowl deflection angle. When the inlets were blocked completely, the resulting spillage disrupted the upper surface vortex flows. Leaving the inlet cowl undeflected resulted in early flow separation on the upper surface and disrupted the adjacent vortex flows.

Two lengthened forebodies, one with a modified cross-sectional shape, were tested in addition to the basic forebody. These alternate shapes were provided by NASA. Asymmetries in the vortex systems generated by each of the three forebodies

were observed in the water tunnel at zero sideslip and high angles of attack. Comparisons with wind tunnel yawing moment data, obtained from unpublished NASA Langley test results, gave good agreement. The forebody vortex patterns in sideslip were examined and their relationship to aircraft lateral/directional stability, as given by the wind tunnel data, was determined. A nose boom was added to each of the three forebodies. The turbulent wake shed from the boom was seen to disrupt the forebody vortices.

INTRODUCTION

The flow field around an aircraft such as the F-15 at high angles of attack is three dimensional and extremely complex. This flow field typically consists of regions of separated, low-energy flow and concentrated vortex flows of high energy. From the results of past investigations (References 1 and 2), it is known that this complex flow can produce aerodynamic characteristics of an airplane which are extremely nonlinear in angle of attack and/or sideslip.

When considering a high angle of attack flight test study of an aircraft such as the F-15, an understanding of the complex fluid flow phenomena present and their effects is desired. If the fluid mechanics which are associated with the nonlinear aerodynamic characteristics of the aircraft can be better understood, a more informative flight test program can be planned. Flow visualization was felt to provide the most comprehensive preliminary evaluation of the vortex flows and the regions of separated flow.

Studies done at Northrop using a water tunnel have provided excellent visualization of vortex flows on wings and fuselage forebodies. The water tunnel has been used to qualitatively define the vortex flow fields on many aircraft configurations. Changes in angle of attack, sideslip, and model configuration can be made quickly and inexpensively using small scale models. The flow visualization results discussed in this report were obtained using a 1/48-scale model of the F-15. All testing was done in the Northrop diagnostic water tunnel which has a test section of 0.41 by 0.61 meters (16 by 24 in.).

The primary purpose of these tests was to determine the vortex flow fields generated above the wing and from the fuselage forebody. Additional

flow visualization studies included testing two lengthened forebodies which were defined by NASA, and investigating the effect of a nose boom on the forebody vortex pair. Several inlet mass flow rates were used and two inlet cowl deflection angles were tested to determine the sensitivity of the vortex flows to these changes. Wherever possible, the water tunnel results are compared to full-scale surface tuft data and to NASA Langley 12-foot low-speed wind tunnel data on a 1/10-scale F-15 model.

SYMBOLS

b	wing span
C_l	rolling moment coefficient
$C_{l\beta}$	lateral stability coefficient, $\frac{\partial C_l}{\partial \beta}$, per deg
C_n	yawing moment coefficient
$C_{n\beta}$	directional stability coefficient, $\frac{\partial C_n}{\partial \beta}$, per deg
d	reference diameter
ℓ	forebody length
M_∞	freestream Mach number
\dot{m}_I	mass flow to inlet
\dot{m}_∞	capture mass flow
$(\dot{m}_I/\dot{m}_\infty)_{\alpha=}$	inlet mass flow ratio at angle of attack
P_T	stagnation pressure
R_d	Reynolds number using base diameter
V_∞	freestream velocity
α	angle of attack
β	angle of sideslip
δ_H	horizontal tail deflection
δ_I	inlet cowl deflection
Λ_{LE}	leading-edge sweep angle

TEST FACILITY AND PROCEDURE

Water Tunnel Facility

The Northrop diagnostic water tunnel is a closed return tunnel used for high quality flow visualization of complex three-dimensional flow fields. The water tunnel is shown schematically in Figure 1. The test section is 0.41 m (16 in.) by 0.61 m (24 in.) by 1.83 m (6 ft.) long and has walls made of transparent plexiglass. The test section is oriented in the vertical direction, which facilitates viewing the model from any aspect. The model is accessed through the top of the tunnel by means of suspension cables connected to the model support system, which slides upward on tracks.

The model support system consists of a sting and sideslip arc which is capable of pitch angles from -10° to 70° , concurrent with a sideslip range of -20° to 20° . The pitch angle can be manually adjusted from the side of the test section. The sideslip angle is preset prior to the model installation.

Test Procedure

The flow visualization in the water tunnel is obtained by injection of colored liquid food dyes having the same density as water. The density of water is 800 times that of air, which gives the dye excellent light reflecting characteristics relative to using smoke in air. The dye is injected into the flow field under a slight pressure. This is accomplished through a remotely-controlled dye probe and through dye tubes internally or externally mounted to the model.

Inlet flows were simulated in the water tunnel by the use of suction through tubes connected to the rear of the exhaust nozzles. The tubes were run to water flow meters outside the tunnel which were used to accurately set a suction rate.

The water tunnel is nominally operated at a test section velocity of 0.09 to 0.12 meters per second (0.3 to 0.4 feet per second). This corresponds to a Reynolds number of 40,000, based on the length of the 1/48 scale F-15 model. The tunnel can be operated at higher velocities, but that requires a higher rate of dye injection for visualization. At the higher tunnel velocities, the motion becomes blurred and the fine details are lost. By having a "slow motion" view of the flow it is easier to follow and can be better understood.

Past Water Tunnel Results

Prior to development of the Northrop water tunnel, the question of whether air flow fields could be properly simulated in water with sufficient accuracy was considered. It is well known that if cavitation is avoided and compressibility effects are negligible, then the fluid motions of water and air at the same Reynolds number are dynamically similar. For the identical model scale and velocity, the Reynolds number in water is higher by a factor of 15 due to the water's greater density. However, because of practical limitations in speed and model scale, water tunnel tests are generally run at Reynolds numbers well below those of wind tunnels. It was found empirically, as shown below, that vortex flows are properly modeled at these lower Reynolds numbers.

Delta Wings

The influence of Reynolds number on the vortex breakdown position of delta wings has been investigated at Northrop and by others. In the Northrop studies (Reference 3), the angle of attack at which vortex breakdown occurred at the trailing edge was observed on delta wings having leading edge sweep angles of 55° to 85° . Figure 2, which is taken from Reference 3, shows that the results obtained in the Northrop water tunnels fall within the range of angles of attack observed by others. The data shown include results from other water tunnels as well as wind tunnels and covers the Reynolds number range of 10^4 to 10^6 , based on root chord. Note that the variation in the data due to Reynolds number is no greater than the variation associated with different facilities and different flow visualization techniques used at the same Reynolds number. The flow visualization studies made by Poisson-Quinton and Werle' (References 4 and 5) have also shown good agreement between flow visualization pictures made at low Reynolds numbers

in water tunnels with those obtained under high-speed flight conditions on full-scale aircraft.

Tangent Ogives

Another vortex flow phenomenon which has been investigated in water tunnels is the formation of asymmetric vortices on bodies of revolution at high angles of attack. The asymmetric forebody vortex flow field generates an asymmetric side force which can produce large yawing moments. Wind tunnel measurements of this side force have been made on tangent ogive-cylinder models of various fineness ratio (References 6, 7, and 8).

The results of Reference 6 show that the angle of attack where a side force first occurs, the onset angle, depends only on body geometry. The more slender the body is, the lower the onset angle. Changes in Reynolds number based on base diameter over the range 0.3 to 3.8×10^6 have been shown to produce no significant change in the angle of onset for a pointed tangent ogive (Reference 7).

To determine the effect of even lower Reynolds numbers, three bodies of revolution were tested in the water tunnel. The bodies consisted of three forebodies of $\ell_F/d = 2.5$, 3.5 , and 5.0 fineness ratio, which were interchangeable with a circular cylinder afterbody of $\ell_A/d = 4.5$. For each body, the angle of attack was noted at which the first shift of the vortices occurred, in height and/or lateral position, away from their symmetric pattern. This observed angle of onset of vortex asymmetry is plotted against total fineness ratio in Figure 3. These results exhibit the same trend and are similar in magnitude to the onset angles of side force which are from wind-tunnel measurements made at a Reynolds number of $R_d = 0.8 \times 10^6$ and Mach number of 0.6 .

MODEL DESCRIPTION

The water tunnel flow visualization studies were conducted with a $1/48$ -scale model of the F-15. A three-view drawing of the model is shown in Figure 4. Particular emphasis was given to the accuracy of the model geometry in the areas of the wing leading edge, inlet lip, and glove leading edge radii. The model

was built with flow-through ducts. To provide the desired inlet mass flow rate, plastic suction tubes were connected to metal tubes which extended aft from the nozzle exits. The installation of the model in the Northrop diagnostic water tunnel is shown in Figure 5. The suction tube for the inlets and the dye supply lines can be seen.

In order to visualize the flow field, the model was equipped with dye injection orifices at the locations shown in Figure 6. Great care was taken in locating the dye orifices to insure that the dye being injected would be entrained into the vortices. A remotely-controlled dye probe was used to survey the model to find the exact location for each orifice. To visualize the wing leading edge vortex, a dye orifice was placed in the leading edge of the wing at the wing-glove junction. For dye to be entrained into the vortex which forms above the glove, a dye tube was run externally on the underside of the glove to a point just outboard and aft of its apex. For the forebody, two internal dye channels extended forward to the apex. The dye orifices were located on both sides of the centerline and flush to the windward surface. The separate channels allow for the use of two colors of dye to help differentiate between left and right forebody vortex patterns. A single dye orifice was located flush to the upper surface of the inlet cowl near the outboard edge.

The model was fitted with two different sets of inlets to permit a change in the inlet cowl deflection angle from 0° to 11° . The horizontal tails could be set to any deflection angle. The production forebody was removable and could be replaced with either of two alternate forebody shapes. The two alternate forebodies were a long forebody shown in Figure 7 and a cambered forebody shown in Figure 8. Each of the forebodies was able to accept a nose boom. The installation of the nose boom on each forebody is shown in Figure 9. A wire of 0.089 cm diameter was attached to the long forebody in the helical pattern shown in Figure 10 to form a separation trip for some of the tests.

RESULTS AND DISCUSSION

The experimental results that were obtained consist of a set of photographs documenting the water tunnel flow visualization studies. Selected

results are referred to in the text and are given at the end of this report. The water tunnel results are compared to the results of a tuft study done on a full-scale F-15 by NASA DFRG. Whenever possible, comparisons are made between the water tunnel flow visualization results and force and moment data obtained in the NASA Langley 12-foot low-speed wind tunnel using a 1/10-scale F-15 model.

Wing Flow Field Characteristics

The baseline configuration for this study is with the production forebody, the horizontal tail deflected to $\delta_H = -29^\circ$, and the inlet cowl deflected to $\delta_I = 11^\circ$. The inlet mass flow ratio was set to simulate the inlet conditions at a free-stream Mach number of 0.3. This mass flow ratio at 0° angle of attack is $(\dot{m}_I/\dot{m}_\infty)_{\alpha=0} = 1.85$. The variation of inlet mass flow ratio with free-stream angle of attack for several freestream Mach numbers is given in Figure 11.

The dye orifices in the leading edge of the wing at the wing-glove junction and the pair of orifices on the underside of the gloves are located such that the dye from them would be entrained into the vortices. At 5° angle of attack, however, the flow is fully attached on the upper surface. The dye from the underside of the glove is pulled to the upper surface by the upwash ahead of the wing and the lower pressure on the upper surface. This dye is within the boundary layer and Figure 12 shows that the surface flow is in the chordwise direction but with some spanwise spreading. The dye from the wing-glove junction follows a streamline above the surface of the wing and moves chordwise. The difference in the direction of the surface flow and the external flow above the surface is plainly seen.

As seen in Figure 13(a), the wing leading-edge vortex begins to form at 10° angle of attack. At this angle, the vortex is rather weak and diffuse. A diffuse vortex aft of the glove is also beginning to form above the upper surface of the wing. The dye from the wing-glove junction is being entrained into both the wing leading-edge vortex and the glove vortex. The dye flowing aft over the glove is swept outboard and underneath the leading-edge vortex. This dye spreads out over the wing and collects between the wing vortex and the wing leading edge. This indicates the beginning of a secondary separation which occurs outboard of the core location of the wing vortex. This secondary separation line has often been seen on the surface of delta wings, as in Reference 9. The secondary separation line can be seen in Figure 13(a) to curve

away from the leading edge, finally turning streamwise. The primary separation line is the leading edge of the wing where the feeding sheet of the wing vortex originates. The portion of the wing outboard of where the leading-edge vortex forms is stalled with flow separation occurring at the leading edge. The flow on the upper surface of the glove and inlet cowl is attached and moves streamwise until it is swept outboard by the induced velocity of the leading-edge and glove vortices.

At 12° angle of attack, a well defined wing and glove vortex are formed as shown in Figure 12. The concentrated core of the wing vortex can be seen to flare out at the vortex breakdown point. After the breakdown or burst, the turbulent flow turns toward the freestream direction. The secondary vortex is faintly seen emanating from the wing-glove junction and following a path between the wing leading edge and the primary vortex core location.

By 15° angle of attack, Figure 13(b), the glove vortex is tightly rolled up and still moves in the freestream direction to the vertical tails where it breaks down. The glove vortex is higher above the surface of the wing than is the wing vortex as seen in a profile view. The wing vortex in Figure 13(b) moves aft from the wing leading edge at a constant angle until it bursts. The dye from the burst vortex spread outboard into the separated wing region but none moved inboard where the wing had not yet stalled. The burst point of the wing vortex moves farther forward when the angle of attack is increased from 12° to 15° . At the same time, the vortex burst occurs farther inboard. Soon after the vortex burst, the turbulent flow turns streamwise and this, too, occurs farther inboard with increasing angle of attack.

The dye on the upper surface of the inlet cowl at 15° angle of attack indicates a region of reversed flow near the lip of the cowl. The dye is flowing forward into this region and then separating from the surface. Downstream of this region, the surface flow is attached and moving aft until the induced spanwise flow from the glove and wing vortex sweeps the flow outboard.

Between 15° and 20° angle of attack, the burst point of wing vortex continues to move forward as more and more of the wing panel becomes separated.

The wing vortex at 18° can be seen to persist only a short distance before breakdown occurs (Figure 12). The glove vortex has burst before reaching the vertical tail. As evidence of the increased spanwise flow on the wing, the glove vortex is seen to curve outboard before breaking down. The induced velocity of the leading-edge vortex and glove vortex creates a spanwise flow over the inboard surface of the wing. As shown in Figure 13(c), at 20° angle of attack the burst point of the leading-edge vortex has moved to the wing-glove junction and the wing panel has become completely separated. The glove vortex turns outboard slightly and breaks down when it reaches the low velocity, separated flow above the wing panel. The dye from the orifice on the upper surface of the inlet cowl showed that area to be separated at 20° angle of attack.

The flow field at 25° angle of attack is presented in Figure 13(d). The leading-edge vortex has burst and its induced effect of increasing the spanwise flow is no longer observed. The glove vortex no longer turns spanwise but instead moves aft and bursts sooner than at the lower angles of attack. The low velocity and reversed-flow region behind the stalled wing panel causes the axial velocity within the core of the vortex to stagnate. When this occurs, there is a rapid expansion of the vortex to a larger, turbulent flow. This vortex breakdown or bursting is clearly seen in Figure 13(d). After breakdown, the dye spreads outboard but the inner region above the fuselage remains free of entrained dye.

When the angle of attack is increased to 30° (Figure 12), the glove vortex becomes diffuse and not well defined. The pair of vortices continues to move streamwise but burst soon after the wing-glove junction. The glove vortices pass above the glove and do not burst until they reach the wing wake. For angles of attack of 35° and above, a vortex is no longer formed above the glove but is replaced by a turbulent wake.

Full-Scale Tuft Study

A tuft study was conducted by NASA DFRC on an F-15 aircraft in flight at 0.3 Mach number, a Reynolds number of $3.9 \times 10^6/\text{meter}$ ($1.19 \times 10^6/\text{ft}$) and normally zero sideslip. Movies were taken from a chase aircraft and the results were summarized

by NASA in the series of sketches shown in Figure 13. The sketches divide the observed flow patterns into 3 types of flows; attached flow, attached but unsteady flow, and separated and/or reversed flow. The direction of the surface flow is shown by the tufts in the photographs of Figure 14. These still photographs were made from the movie.

As shown in Figure 14, at 5° angle of attack the flow on the surface of the wing is attached everywhere and all of the tufts are pointed in the streamwise direction. The flow visualization in the water tunnel in Figure 12 at 5° angle of attack shows attached flow moving streamwise. As can be seen in Figure 13(a), at 10° angle of attack the outboard portion of the wing and along the leading edge of the wing has separated flow. Some of the tufts in Figure 14 at 12° angle of attack can be seen to be pointing forward, indicating the reversed flow within the separated region. On the inboard portion of the wing the tufts are still lined up in the streamwise direction. The boundary between the separated flow and the unsteady flow is a line at a constant angle from the leading edge until it turns and runs streamwise. From studying the flow field seen in the water tunnel at 10° and 12° (Figure 12), it can be seen that this boundary coincides with the secondary separation line which forms between the wing leading edge and the wing vortex core location. The path of the wing primary vortex is above the unsteady flow region. The flow patterns turn streamwise after the wing vortex burst. The flow beneath the glove vortex is attached and becoming unsteady in places.

The tuft patterns at 15° angle of attack are presented in Figure 13(b). The boundary between the separated flow and the unsteady flow has shifted farther inboard. This corresponds to the shift in the leading-edge vortex burst point farther inboard. With the vortex bursting farther inboard, the flow after the burst is turned streamwise at a more inboard station. The vortex burst point observed in the water tunnel is very close to the point where the tuft pattern turns streamwise on the wing. The tuft patterns indicate that at 15° , the flow inboard and downstream of the leading-edge vortex is unsteady but not separated. It is known that flow reattachment can occur downstream of the vortex (Reference 9) and that the induced effect of the leading-edge vortex is to reduce the angle of attack over the inboard sections of the lifting surface (Reference 10). The flow on the glove itself at 15° is shown as being separated, which agrees with the water tunnel results which show the glove vortex being formed by leading-edge separation along the edge of the glove.

Between 15° and 20° angle of attack the surface flow direction becomes less streamwise and increasingly spanwise as indicated by the tufts. Figure 14 shows the surface flow at 18.5° . Near the fuselage centerline the flow is streamwise but going farther outboard the tufts are directed more and more spanwise. A similar pattern is seen in the water tunnel at 15° (Figure 13(b)) where the dye on the inlet cowl is swept outboard beneath the glove and wing vortices. The glove vortex itself begins to move outboard for angles of attack above 15° .

At 20° angle of attack the flow regions given in Figure 13 (c) show that the entire wing panel is separated and there is no evidence of any leading-edge vortex. The water tunnel photograph shows that at 20° the leading-edge vortex has completely broken down. The tufts show the region beneath the glove vortex to be separated, but the glove vortex does not burst until it reaches 50% of the wing root chord. The reason that this vortex can persist downstream is that it raises above the surface of the wing, as seen in Figure 17. Due to its height above the wing, its induced effect of creating spanwise flow is reduced but the vortex can provide additional lift due to the low pressure associated with it. As shown by the tuft patterns, there is still unsteady flow inboard of the wing root and over the upper rear of the fuselage.

For 25° angle of attack the tufts indicate a large region of separated flow over the wing and forward half of the fuselage, with unsteady flow on the rear portion of the fuselage. The flow visualization done in the water tunnel at 25° shows the glove vortex breaking down sooner at this higher angle of attack. The wake from the separated wing extends higher above the wing when the angle of attack is increased and the glove vortex enters the wake sooner. After the vortex bursts, it spreads outboard into the separated flow above the wings, but not inboard where there is still only unsteady flow above the fuselage.

The tuft photo in Figure 14 shows the complete flow separation and reversal on the wing panel at 24° angle of attack. Little tuft data exist above 24° but it was noted that on the rear of the fuselage no flow reversal or separation is seen at the higher angles tested. From the unpublished Langley wind tunnel data, it is known that the aircraft stall does not occur at 20° when the wing stalls but instead occurs above 35° when the broad, flat fuselage become completely stalled and the glove vortex has burst completely.

Inlet Mass Flow Effects

In order to determine the effect of changes in inlet mass flow ratio on the upper surface flow field, several mass flow ratios were tested. The baseline configuration, which was already discussed under the wing flow field characteristics, is the mass flow ratio for a freestream Mach number of 0.3, the military power setting, and inlet cowl angle of 11° . These conditions are nominally equivalent to what was flown by NASA DFRC during the tuft studies on the actual aircraft. The variation of inlet mass flow ratio with freestream angle of attack for several freestream Mach numbers is given in Figure 11. For the 0.3 Mach number, the mass flow ratio at 0° angle of attack is $(\dot{m}_I/\dot{m}_\infty)_{\alpha=0} = 1.85$ and the inlet is pulling air from an area larger than the capture area of the inlet. As the angle of attack is increased, more inlet area is presented to the freestream but the engines are still pulling the same volume of flow. Once the mass flow ratio is less than one, the engine cannot take all of the flow coming to the inlet, the excess "spills" from the inlet and moves around the lower cowl and side wall of the inlet. This spillage begins at 16° angle of attack for the 0.3 Mach number condition simulated.

The second mass flow rate tested was to simulate a freestream Mach number of 0.2 inlet conditions. At 0° angle of attack the mass flow ratio is $(\dot{m}_I/\dot{m}_\infty)_{\alpha=0} = 2.48$, which means that a larger volume of flow is entering the inlet at this lower Mach number. The inlet does not begin to spill until above 30° angle of attack for the 0.2 Mach number simulated condition.

The wing flow field for the 0.2 Mach number inlet conditions is shown in Figure 15. At 10° , 12° , and 15° angle of attack, the higher inlet mass flow rate has no apparent effect on the upper surface flow field. At 18° angle of attack and above, the glove vortex is better defined and more tightly rolled up for the higher flow rate condition. As was mentioned before, spillage from the inlet at the 0.3 Mach number conditions can begin above 16° angle of attack. The flow which must pass around the inlet is at an angle of attack to the vertical side wall of the inlet. This side wall has a sharp leading edge and flow separation occurs at this edge. The separated, turbulent flow on this side wall is just forward and below the glove. The unsteady flow disturbs the formation of the glove vortex making it loosely rolled up and less concentrated. At 18° there is also an apparent increase in spanwise flow with the higher inlet flow rate, as the glove vortex turns sharply outboard before breaking down.

As the angle of attack is increased beyond 18° , no difference in spanwise flow is seen. Under the higher flow rate, the glove vortex continued to be better defined and more tightly rolled up through 30° angle of attack. At 35° much spillage is occurring with both inlet flow rates and the glove vortex is replaced by a turbulent wake.

After testing the inlet with a flow rate higher than the baseline conditions, the model was tested without flow through the inlets. This configuration was of great interest because the remotely piloted 3/8-scale F-15 model used by NASA-DFRC has blocked inlets. On the water tunnel model, the inlets were not physically blocked but the suction was shut off, preventing any flow.

At 5° angle of attack, the upper surface flow appeared the same as for the baseline flow rate of $(\dot{m}_I/\dot{m}_\infty)_{\alpha=0} = 1.85$. By 10° the glove vortex was beginning to form but it was rather weak and diffuse, as seen in Figure 16. No wing vortex can be seen. A glove vortex is still being formed at 12° angle of attack but it is diffuse and unsteady. A weak vortex at the wing leading edge is seen intermittently but for the majority of the time, the wing vortex is destroyed by the turbulent flow coming aft from the blocked inlet and over the wing.

The glove vortex is no longer formed at 15° and the flow above the glove resembles the baseline configuration at 35° where a turbulent wake comes from the glove. A wing leading-edge vortex is seen but it breaks down farther forward than before and was often burst completely. At 18° there is no vortex flow above the upper surface of the wing. Most of the flow off the wing goes streamwise with almost no spanwise flow. As the angle of attack is increased further, the dye beneath the glove is pulled upstream along the side wall of the inlet into the large, separated region. Figure 17 compares the profile view of the inlet for the zero mass flow case and the baseline mass flow rate. The additional dye being pulled forward and the disruption of the glove vortex is evident. The results of the tuft study conducted by NASA DFRC at 0.3 Mach number show separated flow on the side wall of the inlet at 20° angle of attack. The movement of the tufts increases at higher angles of attack as the spillage increases.

Sideslip Effects

Through the use of the sideslip arc, the model could be set at a sideslip angle while it remained centered within the tunnel test section. The model was first set to 5° sideslip and the angle of attack was varied from 5° to 35° . The sideslip angle was increased to 10° and the angle of attack sweep was repeated. The flow patterns observed at 10° sideslip are similar to the flow patterns at 5° sideslip and, therefore, only the results for 10° of sideslip will be discussed. Photographs of the wing flow field for a sideslip angle of 10° over an angle of attack range of 10° to 25° are presented in Figure 18.

At 10° angle of attack, the wing leading-edge vortices and the windward glove vortex are beginning to form. By 15° angle of attack, both the left and right wing and glove vortices are well formed. The left and right glove vortices pass their respective vertical tails on the leeward side whereas at 0° sideslip, they impinged on the leading edge of the verticals. A difference in both the path and burst point between the windward and leeward wing leading-edge vortices is evident.

In the sideslip attitude, the leeward wing has an effectively higher sweep angle. This higher sweep increases the axial velocity within the vortex core at the expense of the rotational velocity. This increases vortex stability while reducing the strength. With its increased stability, the leeward vortex moves farther aft before bursting.

On the windward wing, the sweep angle has been effectively reduced, which reduces the axial velocity of the vortex while increasing the rotational velocity. The velocity normal to the wing quarter chord is greater on the windward wing. The path of both the wing vortices has been shifted to the leeward side.

By 20° angle of attack, the burst point of the windward vortex has moved to the apex of the wing and the wing is stalled. The leeward wing vortex with its greater stability has a much slower movement in its burst point as the angle of attack is increased. This difference in vortex burst point due to sideslip has been observed to occur with vortices formed by a leading edge extension on other fighter aircraft (Reference 2) as well as on delta wings (Reference 9).

The vortex formed above the glove appears to behave in a manner opposite to the leading-edge vortices. At 20° , the windward vortex above the glove is well defined and even the secondary vortex is clearly seen between the primary vortex and the leading edge. On the leeward side, however, the glove vortex is very diffuse. This is due to the separated flow on the side wall of the inlet which is located forward and below the glove. With the combination of flow angle due to sideslip and that due to spillage from the inlet, there is flow separation at the sharp leading edge of the inlet side wall. The turbulent flow from this separated region moves aft over the glove and disrupts the formation of the glove vortex. On the windward side, the freestream flow is toward the side wall and the flow remains attached there.

It is of interest to note the curvature of the glove vortex outboard before the burst. After the burst, the dye could be seen to move outboard and even forward. The dye is being pulled into the region of low velocity and reversed flow behind the stalled windward wing.

A vortex is no longer formed above the leeward glove at 25° angle of attack. The burst point of the windward glove vortex has moved farther forward. Again the flow aft of the burst can be seen to be outboard toward the wing tip. The flow angle is no longer toward the center of the fuselage as was the case at low angles of attack when the sidewash resulted from the sideslip angle. This "adverse" sidewash at high angles of attack, along with a reduction in the dynamic pressure at the vertical tails, has been observed on other swept-wing fighters and is discussed in Reference 1. When the angle of attack was increased above 25° , the burst point of the windward glove vortex continued to move forward until 35° , when only a turbulent wake was seen above the glove.

Presented in Figure 19 are data, as yet unpublished, from a NASA-Langley 12-ft. low-speed wind tunnel test of a 1/10-scale F-15 model. The model has flow-through inlets and was tested with an inlet cowl deflection of $\delta_I = 12^\circ$ and horizontal tail deflection of $\delta_H = 0^\circ$. The tests were made at a Reynolds number of 1.28×10^6 per meter (0.39×10^6 per foot). The data in Figure 19 were obtained with and without the twin vertical tails on the aircraft configuration with the long forebody. The stability derivatives were obtained over a sideslip range of $\pm 5^\circ$. The data illustrate the effect of the twin vertical tails on

directional stability, $C_{n\beta}$, and lateral stability, $C_{l\beta}$. As the angle of attack is increased, the vertical tails become immersed in the low-velocity wake of the stalled wing. The resulting reduction in directional stability with increasing angle of attack is evident. Above 30° angle of attack, the contribution of the vertical tails produces a further reduction in the directional stability than with tails off. The vertical tails are actually destabilizing at high angles of attack. This would support the observations made in the water tunnel of adverse sidewash near the windward tail at high angles of attack.

In the water tunnel at 20° angle of attack, the windward wing was seen to be stalled while a vortex was still present on the leeward wing. The leeward wing would then be generating greater lift and a destabilizing rolling moment results. This causes the loss in effective dihedral seen above 20° angle of attack in the wind tunnel lateral stability data.

The side force produced by the vertical tails acts through a vertical moment arm to produce a rolling moment. When the vertical tail is producing a stable yawing moment at the lower angles of attack, a stable rolling moment is produced as well. At the higher angles of attack, when the vertical tails are directionally destabilizing, they also reduce the effective dihedral. The stabilizing contribution to the dihedral effect from the glove vortex on the windward side would decrease with increasing angle of attack as its burst point progresses to the apex of the glove.

The unpublished Langley wind tunnel data showed that the effect of deflecting the horizontal tail to $\delta_H = -25^\circ$ was to cause the model to become directionally unstable at 18° angle of attack compared to 21° for $\delta_H = 0^\circ$. The deflection of the horizontal tail also produced unstable values of $C_{l\beta}$ between 30° and 35° angle of attack. Most of the testing done in the water tunnel was done with the horizontal tail deflected to $\delta_H = -29^\circ$, as this large deflection would be needed to reach high angles of attack in flight. Much of the water tunnel study concentrated on the higher angles of attack, particularly the study of forebody effects where the angle of attack ranged from 20° to 55° . The aerodynamic phenomenon responsible for the loss in lateral stability due to deflecting the horizontal could not be determined in the present water tunnel studies. This loss in stability occurs in an angle of attack region where both wing panels are completely stalled. Dye patterns under these conditions are largely diffused and difficult to interpret. The majority of

the wind tunnel data that are available for comparison to the water tunnel studies were taken with the horizontal tails undeflected, $\delta_H = 0^\circ$. For this configuration, the wind tunnel data still clearly show the effect on stability of other changes in the aircraft configuration. This wind tunnel data will be used as a base for comparison to the flow visualization done in the water tunnel.

The pitch sweep at 10° sideslip was repeated with the suction to the inlets turned off. This configuration is representative of the 3/8-scale F-15 RPRV which has blocked inlets. At 5° angle of attack, the upper surface flow was attached and the flow patterns are the same as for the baseline flow rate of $(\dot{m}_I/\dot{m}_\infty)_{\alpha=0} = 1.85$. At 10° , as seen in Figure 20, the glove vortex is beginning to form and spanwise surface flow is evident on the leeward wing. The windward wing and glove vortices are well formed at 15° angle of attack, but no vortex flow is seen on the lee side. The spillage from the blocked inlet and the separation on the inlet side wall generate a turbulent wake which moves downstream and onto the wing, where it disrupts the vortex formation. In contrast to this, with the baseline flow rate conditions (Figure 18), both vortices are formed on the leeward side. At 20° angle of attack, the leading-edge vortex does form on the leeward side. It could be seen in a profile view that the turbulent flow from the inlet area is passing above the wing and does not interfere with the wing vortex.

An effect from having the inlets blocked is seen on the windward side at 20° . The windward glove vortex is much weaker and breaks down farther forward than in the baseline case. The spillage from the blocked inlets has eliminated all vortex flows at 25° angle of attack while for the baseline inlet flow rate, the glove vortex is still present on the windward side at 30° angle of attack.

An additional effect that is related to inlet mass flow but was not investigated is the effect of engine exhaust. The inlet mass flow was seen to improve the flow on the forward portion of the upper surface, especially above the glove. The engine exhaust jet should have a similar effect on the rear of the fuselage. The flow entrainment into the exhaust jet would help keep the flow attached on the upper rear of the fuselage to higher angles of attack. The tuft study results shown in Figure 13(d) at 25° angle of attack indicates that the flow on the aft half of the fuselage was unsteady but no reversed or separated flow was seen. Both the inlet and exhaust flows improve the flow over the top of the fuselage

which would improve the lateral stability at high angles of attack. Engine exhaust flows were not simulated in the water tunnel because the suction tubes for the inlets were run through the exhaust nozzles as shown in Figure 5.

Inlet Cowl Deflection Angle

The effect of having undeflected inlet cowls on the upper surface flow field at 0° sideslip is shown in Figure 21. A comparison to Figure 13(b) reveals some similarity in the flow at 7° angle of attack with $\delta_I = 0^\circ$ and at 15° angle of attack with $\delta_I = 11^\circ$. In both cases there is a separated region of flow just aft of the inlet lip with the dye showing reversed flow and then attached flow farther downstream. On the undeflected inlets, there is separated flow on the inboard portion of the duct at 10° , while the dye remains close to the surface over the glove. At 12° angle of attack, the entire upper surface of the ramp is separated and the reversed flow can be seen at 15° in Figure 21. With the inlet cowl deflection of $\delta_I = 11^\circ$, the separation of the flow on the upper surface is delayed to 20° angle of attack (Figure 13(c)).

The turbulent, separated flow on the upper surface of the inlet cowl has an adverse effect on the glove vortex. The glove vortex appears more turbulent and weaker. At 25° (Figure 21), the glove vortex has been completely disrupted while with $\delta_I = 11^\circ$ it can be seen to be tightly rolled up (Figure 13(d)). The deflection of the inlet appeared to have no effect farther outboard where the wing vortex is unchanged.

By comparing Figure 22 to Figure 18, it can be seen that in sideslip the inlet cowl deflection of $\delta_I = 0^\circ$ has little effect below 20° . The leeward glove vortex is disturbed by the spillage and turbulent flow on the side of the inlet and when the flow is separated on the upper surface, the additional effect is small. On the windward side at 20° angle of attack, however, the separation on the upper surface of the undeflected inlet cowl is seen to affect the windward glove vortex. It is being adversely affected by the separated flow region adjacent to it. When the inlet cowls are left undeflected at 25° angle of attack, the windward glove vortex is replaced by a disordered, separated wake which extends across the upper fuselage.

Presented in Figure 23 are the lateral-directional stability derivatives for the wind tunnel model with a cambered forebody, which illustrates the effect of inlet cowl deflection. A small loss in directional stability between 27.5° and 40° angle of attack resulted for $\delta_I = 0^\circ$ as compared to the $\delta_I = 12^\circ$ case. In contrast to this, there was a large decrease in lateral stability with the undeflected inlet cowls. The sharp loss in $C_{l\beta}$ began at 20° angle of attack. This is also the angle of attack where the first changes in the flow on the windward side were observed in the water tunnel for $\delta_I = 0^\circ$. The values of $C_{l\beta}$ are seen to be unstable over the angle of attack range of 20° to 31°. As already stated, at 25° angle of attack, the flow over the upper fuselage is observed (Figure 22) to be separated and turbulent. The windward glove vortex which is present for $\delta_I = 11^\circ$ is destroyed when the inlets are undeflected. This windward glove vortex has a low-pressure field associated with it which produces a suction force over the surface of the glove. This force acts through a moment arm to the roll axis and produces a stable rolling moment in sideslip.

The undeflected inlets are also seen to have an adverse effect on the flow over the upper fuselage inboard of the glove vortex. The deflection of the cowls would appear to have an effect on the upper fuselage that is similar to deflecting leading-edge flaps on a wing. The deflection of leading-edge flaps has been shown to improve the dihedral effect of several fighter aircraft (References 1 and 2).

Forebody Fineness Ratio Effects

Production Forebody

The first forebody tested in the water tunnel was the production F-15 forebody. The production forebody, shown in Figure 7, has cross-sectional shapes that are elliptical with the major axis vertical just forward of the canopy, but soon transition to a circular shape which continues out to the apex.

The production forebody is the shortest of the three forebodies tested with a forebody fineness ratio of 4.34. This fineness ratio is based on the length of the region ahead of the inlets and the fuselage width in plan view at the inlet station as shown in Figure 4. This is the conventional definition of forebody fineness ratio.

The flow patterns around the production forebody at zero sideslip and selected angles of attack are shown in Figure 24. No vortex flow is observed at 20° angle of attack. The dye flows upward around the sides of the forebody, turns aft, and leaves the surface, becoming turbulent in the separated flow aft of the sharply sloping sides of the canopy. It is not until 30° angle of attack that the vortex pair is formed and the rotating helical pattern is seen (Figure 24). In the profile view at 30° , the boundary layer separation line can be seen where the four dye streaks begin to spread aft. The flow leaves the surface to become a feeding sheet to the forebody vortex. A secondary vortex which forms within the separated flow along the fuselage side can be seen just below the canopy. The primary vortices are symmetrical in position about the aircraft centerline in the plan view and are at identical heights above the aircraft as seen in the profile view.

When the angle of attack is increased to 40° , the strength of the vortex system is noticeably increased as it is more concentrated and the rotational velocity is greater. The profile view at 40° angle of attack in Figure 24 shows that the paths of the streamlines feeding the vortex pair are at a greater angle to the model's horizontal axis than at 30° .

Above 40° the vortex pattern above the forebody develops some slight asymmetries which do not become pronounced until the model is pitched above 50° angle of attack. The asymmetric vortex pattern developed at 0° sideslip and 55° angle of attack is clearly seen in Figure 24. The right side vortex has shifted outboard and upward, away from the surface. The vortex on the left side remains close to the body and has shifted inboard to where it is above the fuselage centerline near the canopy.

The force generated by the forebody will no longer be just a normal force but will be biased to one side as a result of the shift in the vortex pattern. The vortex which remains closer to the side of the forebody will exert a stronger force than the one that has moved up and outboard. A net sideforce will result toward the vortex that remains close to the body.

In Figure 26, the yawing moment at zero sideslip is shown for the production forebody. The yawing moment can be seen to be increasing for angles of attack greater than 50° . This onset angle of attack of the asymmetric yawing moment is

higher than for the tangent ogives of similar fineness ratio shown in Figure 3. This is typically the case for aircraft configurations as is shown in Reference 7. The magnitude of the asymmetric yawing moment is consistent with previously measured data on similar configurations (Reference 7).

The flow-field patterns around the production forebody at 5° of sideslip for 30° and 50° angle of attack are shown in Figure 25. At 30° angle of attack, a shift in the vortex pattern is evident when compared to the symmetrical pattern seen at zero sideslip (Figure 24). In the profile view of the leeward side, the secondary vortex has shifted to a position lower down on the side of the fuselage relative to its position at zero sideslip. A shift in the location of the stagnation line on the underside of the forebody is indicated. Also evident in the profile view is that the windward vortex is higher above the surface of the forebody than the leeward vortex. In the plan view, it can be seen that in sideslip the windward vortex has shifted to a position higher up on the side of the fuselage and closer to the fuselage centerline. The leeward vortex is displaced to a position lower and closer to the side of the fuselage.

When the angle of attack was increased to 50° at 5° of sideslip, the arrangement of the vortices is seen to be similar to that at 30° angle of attack but with the strength of both vortices increased. The windward vortex remains high above the surface while the leeward vortex remains close to the body over a considerable length. In the plan view, the higher, windward vortex can be seen to pass above the burst leeward vortex.

The directional stability for the production forebody configuration is shown in Figure 26. The initial loss in directional stability was discussed previously and is attributed to the vertical tail becoming immersed in the low-velocity wake of the wing. This low-velocity wake above the stalled wing can be seen in Figures 24 and 25. When the nose vortices move aft of the canopy and encounter the lower velocity flow, there is a deceleration of the flow along the axis of the vortex and a stagnation in the core, resulting in the vortex burst. This bursting of the forebody vortex pair occurs above the wing and forward of the vertical tails.

At the higher angles of attack, the forebody vortex pair which forms will affect the directional stability of the aircraft. This results from the vortices producing a side force on the forebody, as was shown in Reference 1, rather than an interaction with the vertical tails. Whether this effect is stabilizing or not depends on the strength and orientation of the vortices around the forebody. As can be seen in Figure 26, the configuration with the production forebody is directionally unstable with little change in the level of this instability from 30° to 50° angle of attack. As was seen in the water tunnel flow visualization (Figure 25), in a sideslip attitude the leeward vortex remained close to the body while the windward vortex was further away. This vortex orientation produces a net sideforce which tends to pull the forebody further out of alignment with the freestream. This is an unstable yawing moment which is responsible for the negative directional stability seen in the data of Figure 26 at high angles of attack.

The flow field around the production forebody was also observed with and without mass flow through the inlets. Figure 27 compares the production forebody flow field at 20° and 40° angle of attack with the baseline flow rate of $(\dot{m}_I / \dot{m}_\infty)_{\alpha=0} = 1.85$ to the blocked inlet conditions. In the profile views at 20° angle of attack, there is no apparent change in the flow pattern forward of the inlet due to the change in inlet flow rate. Aft of the inlet where the flow separates from the canopy, the wake is the same in both cases. A comparison was made of the plan views at 20° angle of attack (not shown) and no effect of inlet flow rate was observed. The profile views at 40° angle of attack show that the inlet flow rate has no effect on the boundary layer separation line or on the formation of the primary or secondary vortices. Downstream of the inlet there is no change in the path of the vortex. The plan views at 40° angle of attack were compared (not shown), and again no effect of the inlet flow rate on the forebody flow field was seen. Since the results of this short study showed no apparent effect from having blocked inlets, the majority of the forebody studies done in the water tunnel were conducted with blocked inlets.

A comparison is shown in Figure 28 of the surface flow on the production forebody in flight and in the water tunnel. Both the full-scale aircraft and the 1/48-scale model were at 20° angle of attack and zero sideslip. The tuft data were obtained at $M_\infty = 0.30$ and a Reynolds number of approximately $3.9 \times 10^6/\text{meter}$ ($1.19 \times 10^6/\text{foot}$). The water tunnel flow visualization was performed at a Reynolds number of $0.1 \times 10^6/\text{meter}$ ($0.03 \times 10^6/\text{foot}$). The direction of the surface flow on

the full-scale aircraft is shown in a single frame extracted from the flight test movies made by NASA DFRC and reproduced here. There is good qualitative agreement in the flow direction on the forebody as shown by tufts in flight and the dye used in the water tunnel. The results of the tuft study conducted by NASA DFRC indicated a region of separated flow at the rear of the canopy. The dye in the boundary layer of the water tunnel model is seen to flow aft along the side of the canopy and then separate near the rear of the canopy. The dye continues downstream in a turbulent wake.

Long Forebody

The profile, plan, and cross-sectional views of the long forebody are shown in Figure 7. The cross-sectional shapes of the long forebody are identical to the production F-15 forebody but are spaced at wider intervals along the fuselage length. The forebody fineness ratio for the long forebody is 5.68 whereas the production forebody is 4.34. The increased length of this forebody increases the strength of the vortex system when compared to the production forebody already discussed.

The flow patterns around the long forebody at zero sideslip and selected angles of attack are shown in Figure 29. The vortex system forms earlier on the long forebody. The vortex system on the long forebody at 25° angle of attack is as fully developed as the system on the production forebody was at 30° angle of attack. In the profile view at 35° angle of attack, the two primary vortices are seen to be at equal heights above the upper surface of the fuselage. The vortices can be seen to be symmetrical about the aircraft centerline in the plan view. From 35° to 40° the vortex pair begins to shift to an asymmetric pattern. The left side vortex is displaced outboard and upward, away from the surface. The vortex on the right side remains close to the body and is curving inboard near the canopy. In the profile view, the asymmetry in heights is evident at 50° angle of attack.

As the angle of attack is increased further, the asymmetry at zero sideslip becomes more pronounced. At 50° angle of attack, a large asymmetry in the path of vortices is shown in Figure 29. The difference in both height and lateral position is greatly increased when compared to 40° angle of attack. The left vortex

turns away from the surface and continues on downstream without bursting. The feeding sheet to this vortex is broken as its distance above the nose increases. The dye from the last two dye ports never reaches the vortex. The right side vortex remains close to the surface of the forebody until near the canopy when it turns upward.

As shown in the wind tunnel data in Figure 26, the model with the long forebody does exhibit large asymmetric yawing moments. The onset angle of attack is 35° and the magnitude of the asymmetry increases sharply as the angle of attack is increased. The relationship between the asymmetric vortex pattern and the yawing moments is clearly shown by the water tunnel visualization. The asymmetry in the vortex pattern is first observed in the water tunnel between 35° and 40° angle of attack. With increasing angle of attack, the observed asymmetry becomes much more pronounced. The magnitude of the maximum yawing moment for the long forebody as measured in wind tunnel tests is approximately double the magnitude measured for the production forebody. The flow patterns observed in the water tunnel illustrate that the vortex system emanating from the long forebody are more asymmetric in nature when compared to the production forebody. The trends observed in the water tunnel correlate well with the wind tunnel data.

The flow field patterns around the long forebody at 5° of sideslip and selected angles of attack are shown in Figure 30. At 35° angle of attack, a shift in the vortex pattern is evident when compared to the symmetrical pattern seen at zero sideslip (Figure 29). In the profile view, the windward vortex is higher above the surface of the forebody than the leeward vortex. In the plan view, it is seen that in sideslip the windward vortex has shifted to a position higher up on the side of the fuselage and closer to the fuselage centerline. The leeward vortex has moved to a position lower down and closer to the side of the fuselage. This vortex pattern is very similar to what was observed on the production forebody in sideslip. When the angle of attack is increased to 40° at 5° of sideslip, the arrangement of the vortices is seen to be similar to that at 35° angle of attack. The strength of both vortices is increased at the higher angle while the height of the windward vortex above the surface has increased. The leeward vortex remains close to the body.

When the angle of attack is increased to 45° , the vortex patterns are observed to become completely reversed from what the patterns had been at 40° . It is now the leeward vortex that is higher above the surface while the windward vortex remains close to the surface over its entire length. In the plan view, the leeward vortex has shifted outboard, away from the surface. The windward vortex has moved inboard above the aft portion of the canopy. When the angle of attack was increased from 45° to 50° , the vertical and lateral displacement of the vortices became more pronounced.

The observed water tunnel flow patterns can be correlated with the wind tunnel measured directional stability for the long forebody configuration. At low angles of attack, the forebody is directionally destabilizing because of its side area ahead of the center of gravity. When the angle of attack is increased above 20° , the vortices form above the forebody and, depending on their strength and orientation, can add to or overcome the directionally destabilizing effect of the forebody side area. The long forebody configuration is shown in Figure 26 to become increasingly unstable up to 40° angle of attack. As discussed in the preceding paragraphs, this loss in stability can be attributed to the orientation of the forebody vortices. Below 40° angle of attack, the leeward vortex remains close to the body while the windward vortex is away from the surface. This orientation results in a side force which acts through the long moment arm to produce a destabilizing yawing moment. This is added to the directionally destabilizing effect of the forebody side area. Above 40° angle of attack, the wind tunnel data for the long forebody configuration show a sharp reduction in the level of directional instability. This is due to a shift in the forebody vortices into a pattern which produces a less destabilizing yawing moment. The windward vortex moves closer to the forebody while the leeward moves away to produce a net side force which tends to pull the aircraft forebody back into alignment with the freestream. This restoring side force was, however, never strong enough to overcome the destabilizing effects and reach positive directional stability.

Also shown in Figure 26 is the lateral stability parameter, $C_{l\beta}$. The long forebody configuration shows a loss of effective dihedral above 20° angle of attack which is greater than for the production forebody. This suggests that the long forebody vortices influence the wing or vertical tail flow fields. At zero

sideslip the long forebody was observed in the water tunnel to have no apparent effect on the wing flow-field, but that may not be the case for 5° of sideslip.

Forebody Cross-Sectional Shape

Cambered Forebody

The profile, plan, and cross-sectional views of the cambered forebody are shown in Figure 8. The length and, therefore, the forebody fineness ratio of the cambered forebody is identical to the long forebody. The shape of this forebody, however, is quite different. In the plan view, it can be seen that cambered forebody is broader at the nose with an increased tip radius. In the cross-sectional views, there is a cusp shape on the underside which is deepest at the front and washes out at the furthest aft stations. This cusp gives the tip of the nose a sharp edge. The cross section is more elliptical in shape, with the major axis horizontal, when compared to the long forebody which is more nearly circular.

The flow patterns around the cambered forebody at zero sideslip and selected angles of attack are shown in Figure 31. The forebody vortex pair is observed to be well defined at 25° angle of attack. The profile views show that the dye flows over the ridge at the side of the cusp without separating. The separation line is farther up on the side of the forebody in a location that is similar to the long forebody. The profile view at 40° angle of attack shows a strong, well defined vortex pair, with no difference in height between the vortices. In the plan view at 40° , the vortices are symmetrical in lateral position, and the rotating, helical pattern is clearly seen. The broadness and sharp edge of the tip of the nose strengthen the primary vortices and keep them separated. As discussed previously, the vortices formed by the long forebody were observed to be less stable in position and shift to an asymmetric pattern between 35° and 40° angle of attack. In contrast, the vortex stabilizing effect of the cambered forebody delays the onset of asymmetries in the vortex pattern until 50° angle of attack. As seen in Figure 31, there was a shift in both height and lateral position at this angle. As the angle was increased beyond 50° , the asymmetry remained.

The wind tunnel measured yawing moment at zero sideslip is shown in Figure 26 for the cambered forebody. The variation of C_n with angle of attack shows that the yawing moment builds up to a low level and fluctuates at this low level until

above 50° angle of attack when the yawing moment quickly changes sign along with a change in magnitude. The dramatic reduction in the asymmetric yawing moments when compared to the long, pointed forebody of the same fineness ratio is evident.

The flow patterns around the cambered forebody at 5° of sideslip for 30° and 45° angles of attack are shown in Figure 32. At 30° angle of attack a shift in the vortex pattern has occurred when compared to the symmetrical pattern at zero sideslip seen in Figure 31. The windward vortex is closer to the surface of the forebody while the leeward is raised. The windward vortex has also shifted closer to the fuselage centerline while the leeward vortex has moved outboard. When the angle of attack is increased to 45°, the difference in position between the vortices increases. The windward vortex remains at the same height close to the surface while the leeward vortex moves higher as the angle of attack is increased. The lateral position of the windward vortex at 45° is further inboard while the leeward vortex is displaced outboard and away from the forebody.

In the sideslip attitude, a difference in strength between the leeward and windward vortex is expected. This is similar to the leading-edge vortex on a swept wing in sideslip where the windward vortex becomes stronger. Both vortices increase in strength with increasing angle of attack.

The directional stability of the cambered forebody configuration is shown in Figure 26. This configuration has positive directional stability over the angle of attack range tested. This is a sharp contrast to the results seen for the previous two forebodies tested. The data show a decrease in $C_{n\beta}$ until 23° angle of attack when a steady increase begins. At an angle of attack of 45°, the value of $C_{n\beta}$ is almost three times as large as at 0°. Above 45° the directional stability begins to drop off. Additional, unpublished Langley wind tunnel data, not presented here, show that the large increase in directional stability above 20° occurs at the same time as a large positive change in $C_{y\beta}$. This indicates that the stabilizing yawing moments are produced by a sideforce acting on an area forward of the c.g.

From the water tunnel flow visualization, the large increase in directional stability is seen to be due to the orientation of the forebody vortices. There is an initial loss in directional stability due to a loss of vertical tail effectiveness. As the forebody vortices begin to form, they develop into a

stabilizing pattern which counters the loss. In sideslip, the windward vortex is stronger and it was seen to remain close to the surface as the leeward vortex moves away. This produces a net sideforce which acts through the long moment arm to pull the aircraft back into alignment with the freestream. With increasing angle of attack, this stable yawing moment would increase in magnitude as both the strength of the vortices and their shift in orientation increase. Above an angle of attack of 45° , the directional stability is seen to decrease. At angles of attack above 45° , the windward vortex begins to raise above the surface, turn streamwise, and become diffuse. Other forebodies with a horizontal, elliptical shape provide directional stability and produce a similar vortex pattern (References 1 and 2).

Nose Boom Effects

During flight testing of an aircraft, a large instrumentation nose boom is often used. The nose boom carries flight test instrumentation to determine airspeed, altitude, angle of attack, and sideslip. The installation of a nose boom modifies the nose shape and effectively increases the fineness ratio. A nose boom can significantly alter the flow patterns around a forebody at high angles of attack. A study was made of the effect of a nose boom on the observed vortex patterns of each of the forebodies discussed in the foregoing paragraphs.

Production Forebody

Figure 9 illustrates the nose boom installed on the production forebody. Figure 33 illustrates the effect of the nose boom on the production forebody at zero sideslip. At the lower angles of attack, little change in the flow field is observed. At 35° angle of attack, shown in Figure 33, a change in the forebody flow field is evident when compared to the basic production forebody without a nose boom. The forebody vortex pair is more diffuse, with greater turbulence, and there is some mixing between the two vortices. Through the use of a remote dye probe, it was possible to see that the boom sheds a periodic wake which passes near enough to the forebody vortex pair to cause a disturbance. The alternating vortices moving downstream from the boom are responsible for the alternating pattern seen in the plan view at 35° angle of attack. This alternating mixing between the forebody vortices occurs at the same frequency as the vortex shedding from the nose boom. Under wind tunnel and flight conditions, the nose boom wake would be complete turbulent mixing without the periodic pattern. The periodic vortex shedding occurs only in the range of

Reynolds numbers of about 60 to 5000, based on diameter. During wind tunnel tests, this Reynolds number is at least 20,000.

In the presence of the nose boom, the asymmetric pattern in the forebody vortices onsets at 45° . This asymmetric pattern is shown at 50° angle of attack in Figure 33. A shift in the lateral position of the vortex pair is seen in the plan view. With the addition of the nose boom, the forebody vortices are more diffuse and it is difficult to identify a difference in height between the vortices. The nose boom had no apparent effect on the location of the separation line at any angle of attack but did disrupt the secondary vortices at the higher angles.

The wind tunnel measured yawing moment at zero sideslip is presented in Figure 35 for the production forebody with and without the nose boom. The onset of the asymmetric yawing moments has been lowered from 50° angle of attack for the boom off to 40° for boom on. This is similar to the effect of increasing the forebody fineness ratio as was shown for tangent ogives in Figure 3. Additional, unpublished Langley wind tunnel data not presented here, show no change in the net side force when the boom is added. This indicates a redistribution of the forces farther forward to produce the yawing moment. Both results indicate that the long nose boom on the relatively short production forebody increased the effective fineness ratio.

Figure 34 illustrates the effect of the nose boom on the production forebody at 5° sideslip. At 35° angle of attack the arrangement of the vortex pair is similar to that seen without the nose boom in Figure 24. The windward vortex remains higher above the surface while the leeward is close to the surface in both cases. For 50° angle of attack, the vortex pattern is again similar to the pattern seen without the boom. The wake from the nose boom does cause some disruption of the vortices but on this relatively short forebody the vortices were not strong in the clean configuration.

The directional stability for the production forebody with and without the nose boom is presented in Figure 35. The presence of a nose boom had little effect on the directional stability of the production configuration. The vortex orientation seen in both cases produces a destabilizing yawing moment. The nose boom did reduce the lateral stability above 20° angle of attack, which is also shown in Figure 35.

Long Forebody

Figure 9 illustrates the nose boom installed on the long forebody. Figure 36 illustrates the effect of the nose boom on the long forebody at zero sideslip. The periodic wake from the nose boom is disrupting the forebody vortices, making them more diffuse and causing some mixing between the two vortices. The vortex pattern at 35° angle of attack is symmetric with or without the nose boom. The clean forebody at an angle of 50° produces a very asymmetric vortex pattern, as seen in Figure 29. With the boom on, however, only a small shift in lateral position is seen at 50° and the pattern is similar at 50° angle of attack. No asymmetry in the height of the vortex path can be seen at any angle of attack with the nose boom in place.

The yawing moments at zero sideslip for the long forebody with and without the nose boom are presented in Figure 38. The onset of the asymmetric yawing moment is the same for both configurations. The effective change in fineness ratio due to adding a nose boom to a long forebody is much less than it was for the short forebody. There is little effect from the nose boom below 40° angle of attack where the vortex asymmetries are small and the vortices are close to the body. Above 40° the presence of the nose boom reduces the yawing moment. At 50° angle of attack, the nose boom reduces the level of the asymmetric yawing moment by 50%. Side force measurements, not presented here, show a reduction in side force as well. A nose boom mounted on a 3.5 tangent ogive forebody was shown in Reference 8 to greatly reduce the large side force. The wake from the nose boom reduces the asymmetry in the vortex flow field and weakens the forebody vortices.

The effect of the nose boom on the long forebody at 5° sideslip is shown in Figure 37. At the lowest angles of attack, little change in the flow field is seen. By 30° angle of attack, the disturbance from the nose boom is beginning to alter the vortex flow. The profile view reveals a difference in height between the forebody vortices. The windward vortex is furthest above the surface which is the same orientation seen without the boom. The leeward vortex remains close to the surface through 40° angle of attack for both configurations. Above 40° , a reversal of the vortex pattern began on the clean configuration (Figure 30). No such reversal is seen with the boom on up to the 50° angle of attack tested. The disruptive wake from the nose boom prevents the reversal in the vortex pattern above 40° from developing.

Both configurations undergo a loss in directional stability up to 40° angle of attack. In both cases, the vortex pattern observed in the water tunnel would produce a destabilizing yawing moment. Without the nose boom, there is a sharp reduction in the level of directional instability above 40° angle of attack. This is accompanied by a shift to a less destabilizing vortex pattern as seen in the water tunnel. The wind tunnel model with the nose boom installed continues to lose stability until after 45° . The forebody vortices observed in the water tunnel remain in a destabilizing pattern with the nose boom in place up through an angle of attack of 50° . The addition of the nose boom to the long forebody has little effect on the lateral stability.

Cambered Forebody

Shown in Figure 9 is the nose boom installed on the cambered forebody. Figure 39 illustrates the effect of the nose boom on the cambered forebody at zero sideslip. Without the nose boom at 35° angle of attack, the cambered forebody generates a strong vortex pair with a well defined helical pattern. In the presence of the nose boom, the forebody vortices are diffuse, with more turbulence and reduced strength. A remote dye probe was used to observe the wake from the nose boom above the cambered forebody. The boom was seen to be shedding alternating vortices which travel in a streamwise direction above the forebody vortices. The interaction of this periodic wake with the forebody vortices was greatest near the front where a periodic mixing was seen between the forebody vortex pair. For the clean configuration at 50° angle of attack (Figure 31), a shift in the lateral position of the vortex pair and a difference in height between the vortices occurs. With the nose boom in place, the vortices appear to be symmetric both in position and height. The vortex pair was weaker and diffuse at 50° with the boom on.

The yawing moments at zero sideslip for the cambered forebody with and without the nose boom are presented in Figure 41. The onset of the asymmetric yawing moment is the same for both configurations. With the nose boom added, the zero sideslip yawing moments are reduced in magnitude up to 50° angle of attack. Although not shown, the wind tunnel measured side force was also reduced by the addition of the nose boom. As seen in the flow visualization, the effect of the nose boom is to weaken the forebody vortex pair and to reduce the asymmetry in the vortex orientation around the forebody.

The effect of the nose boom on the cambered forebody at 5° sideslip is shown in Figure 40. When comparing the flow field around the cambered forebody at 30° angle of attack with and without the nose boom, it appears that the wake from the boom is affecting the windward vortex more than the leeward. At 40° angle of attack, the nose boom is causing both the windward and leeward vortices to burst sooner compared to the boom-off case. At 30° , only the windward vortex was breaking down sooner with the boom on. The clean configuration has a greater shift in lateral position of the vortex pair at 50° than is seen in Figure 40 for the boom on case. The profile views at 50° angle of attack show the leeward vortex to be higher in both cases. The addition of the nose boom changes the flow from a tightly rolled up vortex to a diffuse, rotating mass.

The directional and lateral stability for the cambered forebody with and without the nose boom are presented in Figure 41. At all angles of attack of 20° and greater, the addition of a nose boom decreases the level of directional stability. In the water tunnel with the nose boom, the vortices were arranged in a pattern that generates a net sideforce. This sideforce acts through the long moment arm to produce a stable yawing moment. This stable pattern, of the windward vortex remaining close to the body while the leeward vortex moves away, is not as pronounced with the nose boom present. The second major effect of the nose boom is to weaken the vortex pair. The diffuse vortex seen with the nose boom on would not exert the same sideforce on the forebody as a concentrated vortex would. The nose boom decreases slightly the effective dihedral above 25° angle of attack.

Helical Separation Trip

A new device for alleviating the asymmetric yawing moments on high fineness ratio forebodies has been demonstrated by Dr. D. M. Rao. A symmetrical pair of helical, boundary layer separation trips are applied to the forebody to disrupt the vortices. Dr. Rao presents some background information on the helical trips along with some recent experimental results from the NASA Langley 7 x 10 ft. wind tunnel in Reference 11. As part of the forebody research being conducted on the F-15, the helical trips were tested on the long forebody configuration in the NASA Langley 12-ft. low-speed wind tunnel. To provide a qualitative understanding of the effect of the helical trips on the forebody vortices, they were tested on the long forebody in the water tunnel. The arrangement of the helical trips is shown in Figure 10.

The effect of the helical trips on the long forebody at zero sideslip is illustrated in Figure 42. At 35° angle of attack, the helical trips disrupt the feeding sheet to the vortices. The vortices which do form are relatively diffuse. The boundary layer flow is forced to separate at the trip instead of higher up on the forebody along a straighter line. The secondary vortex forms at the same location as on the clean forebody. The primary vortices are symmetrical both in lateral position and in height above the forebody. When the angle of attack is increased to 50° with the helical trips in place (Figure 42), the diffuse vortices remain in a symmetrical arrangement. With a further increase in angle of attack to 55°, a slight asymmetry in the height of the vortices is seen. The clean forebody at high angles exhibits a large asymmetry in vortex position (Figure 29).

The yawing moments at zero sideslip for the long forebody with and without the helical trips are presented in Figure 44. The addition of the helical trips yields a marked reduction in the large asymmetric yawing moment that is present on the clean configuration at angles of attack above 35°. With the helical trips installed, there is a slow build up in yawing moment which is maximum at the highest angle of attack tested, 55°. In the water tunnel, a slight asymmetry is seen at 55° but none was observed at lower angles of attack with the trips on.

The effect of the helical trips on the long forebody at 5° sideslip is shown in Figure 43. A difference in height between the vortices is seen in the profile view in Figure 43 at 35° angle of attack. The windward vortex has shifted higher above the surface than the leeward vortex. The clean configuration at 35° (Figure 30) shows a similar height difference between the vortices. It is of interest to note that the secondary vortex, which normally is accentuated in sideslip, is completely disrupted by the separated flow down stream of the trip. With an increase in angle of attack to 50°, the difference in height between the vortices increases as the windward vortex moves farther away while the leeward vortex remains close to the surface. For the clean configuration, however, the vortex pattern switches above 40° angle of attack and at 50° (Figure 30) the vortices are reversed of what is seen with the trip on.

The directional and lateral stability for the long forebody with and without the helical trips are presented in Figure 44. The helical trip reduces the angle of attack at which $C_{n\beta}$ becomes negative by 2°. With the helical trips on, the configuration is less unstable directionally at the higher angles of attack. The

trips have little effect on the lateral stability. The contribution of the secondary vortices to the directional stability of the configuration is unknown. The primary vortices with the leeward vortex close to the surface, as seen in the water tunnel through 55° angle of attack, would produce a destabilizing yawing moment. The reason for the slight improvement in the directional stability seen in the wind tunnel data with the helical trips on was not apparent in the water tunnel flow visualization.

Wing-Fuselage Underside Vortex

The F-15 has a high wing position and a fuselage side wall that is perpendicular to the wing lower surface. In this corner formed by the wing and fuselage side wall, a vortex is generated when the aircraft is at angle of attack. The vortex rolls up as the incoming flow turns around the lower corner of the fuselage and moves toward the wing. Near the lower surface of the wing some of this flow is turned inward toward the vertical side wall of the fuselage. When the flow encounters the side wall, it is turned upward and the roll up of the vortex is complete.

The vortex which forms at the wing-fuselage junction is shown in Figure 45 at angles of attack of 10° , 20° and 30° . The horizontal tail is deflected to the angle required to hold the aircraft in trimmed flight for each of the three angles of attack. At 10° angle of attack, the vortex is diffuse and does not roll up tight. The vortex moves downstream and passes beneath the horizontal tail where it bursts. With the angle of attack increased to 20° , the vortex gains strength. When the vortex is past the trailing edge of the wing, it moves outboard. The vortex impinges directly on the leading edge of the horizontal tail and breaks down. At 30° angle of attack, the vortex is further increased in strength. The vortex turns outboard just forward of the horizontal tail. With the increased tail deflection, the vortex impinges on the upper surface of the tail and breaks down.

The influence of this underside vortex on the horizontal-tail effectiveness is unknown. The vortex burst and the turbulence downstream of it is a possible cause of vibration of the horizontal tail. Missiles are carried on the lower corner of the fuselage and the underside vortex may interfere with the missile launch, although at low angles of attack the vortex is relatively weak.

CONCLUSIONS

Flow visualization studies were conducted in the Northrop diagnostic water tunnel to provide qualitative definition of the vortex flow fields occurring on a number of F-15 configurations. Details of the wing, glove, and forebody vortex flow fields were obtained over a range of angles of attack and sideslip. The high angle of attack stability characteristics of the configurations measured in a wind tunnel have been correlated to the orientation and structure of the vortex flow fields. Many of the flow visualization results will provide guidance to NASA in planning future 3/8-scale RFRV and full-scale F-15 flight tests. The results will aid in locating pressure taps on the forebody and wing and will be used to identify configurations and angle of attack/sideslip combinations of particular interest for future testing by NASA. The water tunnel flow visualization study aids in interpreting the results of the full-scale tuft study. A summary of the flow visualization results is given below and conclusions are made where appropriate:

1. Both a wing leading-edge vortex pair and a glove vortex pair were formed above the aircraft in its baseline configuration. The burst point of the wing vortex moved forward and inboard rapidly with increasing angle of attack. The wing vortex had completely broken down at 20° angle of attack. This agrees with the full-scale tuft results which showed the entire wing to be stalled at 20° angle of attack. The progression of the glove vortex burst point with increasing angle of attack was much slower than the wing vortex. The path of the glove vortex was found to be relatively high above the surface.

2. The immersion of the vertical tails into the low-energy wake of the stalled wing was clearly seen in the water tunnel and is responsible for the initial loss of directional stability of the aircraft. Some adverse sidewash was seen near the vertical tails and this is an additional destabilizing effect. The results of the water tunnel studies of the aircraft in sideslip indicate that the stall of the leading wing panel is the cause of the loss in effective dihedral above 20° angle of attack.

3. Increasing the inlet mass flow ratio was found to delay inlet spillage to a higher angle of attack and to result in a more concentrated glove vortex. Stopping the inlet flow altogether resulted in spillage at all angles of attack and flow separation on the side wall of the inlet. A turbulent wake from the side of the inlet passed over the top of the wing. This wake caused a serious disruption of all upper surface vortex flows.

4. With the inlet cowls in their undeflected position, the flow on the upper surface of the inlet cowl became separated at a lower angle of attack. This flow separation disrupted the adjacent glove vortex.

5. Increasing the forebody fineness ratio from 4.34 to 5.68 was seen to lower the angle of attack from 30° to 25° at which the forebody vortices were first formed. Increasing the fineness ratio also lowered the angle of attack at which asymmetries were first observed in the forebody vortices from 50° to 35° . Good agreement was found between the water tunnel observations and the wind tunnel measurements of the onset of asymmetries at zero sideslip. At the same angle of attack, the long forebody generated a stronger vortex pair and the vortex asymmetry was more pronounced.

6. The vortex asymmetries seen on the lengthened forebody can be controlled by proper forebody shaping. For the cambered forebody shape ($l/d = 5.68$), no asymmetries were noted in the water tunnel until 50° .

7. Good qualitative agreement was found between the orientation of the forebody vortices at angles of attack and at non-zero sideslip, and the variation of directional stability with angle of attack as measured in the wind tunnel. The cambered forebody was the only forebody tested which produced a vortex pattern in sideslip that would generate a restoring yawing moment at all angles of attack.

8. The addition of the large nose boom to the short production forebody was found to effectively increase its fineness ratio and so reduce the onset angle of the vortex asymmetry. On the longer forebodies, the addition of the nose boom was found to have no effect on the onset angle. At zero sideslip and high angles of attack, the turbulent wake from the nose boom was seen to reduce the asymmetry in

height between the forebody vortices and to reduce the shift in their lateral position relative to the aircraft's centerline. The wake from the nose boom alters the forebody vortex orientations which occur in sideslip and weakens the vortices. These effects were detrimental to the directional stability of the long and cambered forebody configurations.

9. The helical trips on the long forebody were found to disrupt the vortex feeding sheet and result in a pair of diffused vortices which remained symmetrical at high angles of attack and zero sideslip.

10. A large diameter vortex was found to roll up at the wing-fuselage junction. It was seen to impinge on the horizontal tail at the higher angles of attack. It could not be determined what affect this has.

REFERENCES

1. Chambers, J. R. and Grafton, S. B., "Aerodynamic Characteristics of Airplanes at High Angles of Attack," NASA TM 74097, 1977.
2. Headley, J. W., "Analysis of Wind Tunnel Data Pertaining to High Angle-of-Attack Aerodynamics," AFFDL TR-78-94, Volume I, 1978.
3. Erickson, G., "Vortex Breakdown Characteristics of Delta Wings having Leading-Edge Sweep Angles of 55° to 85° ," Northrop Corporation, Aircraft Group, ARR 78-1, 1978.
4. Poisson-Quinton, Ph. and Werle', H., "Water Tunnel Visualization of Vortex Flow," Astronautics and Aeronautics, June 1967.
5. Werle', H., "Hydrodynamic Flow Visualization," Annual Review of Fluid Mechanics, Volume 5, p. 361, 1973.
6. Keener, E. R., Chapman, G. T., and Kruse, R. L., "Effects of Mach Number and Afterbody Length on Onset of Asymmetric Forces on Bodies at Zero Sideslip and High Angles of Attack," AIAA Paper 76-66, 1976.
7. Chapman, G. T., Keener, E. R., and Malcolm, G. N., "Asymmetric Aerodynamic Forces on Aircraft Forebodies at High Angles of Attack - Some Design Guides," Stall/Spin Problems of Military Aircraft, AGARD-CP-199, June 1976.
8. Keener, E. R. and Chapman, G. T., "Onset of Aerodynamic Side Forces at Zero Sideslip on Symmetric Forebodies at High Angles of Attack," AIAA Paper 74-770, 1974.
9. Wentz, W. H., Jr., "Effects of Leading-Edge Camber on Low-Speed Characteristics of Slender Delta Wings," NASA CR-2002, 1972.
10. White, R. P., Jr., Gangwani, S. T., and Balcerak, J. C., "A Theoretical and Experimental Investigation of Vortex Flow Control for High Lift Generation," Office of Naval Research Report ONR-CR212-223-3, 1976.
11. Rao, D. M., "Side-Force Alleviation on Slender, Pointed Forebodies at High Angles of Attack," AIAA Paper 78-1339, 1978.

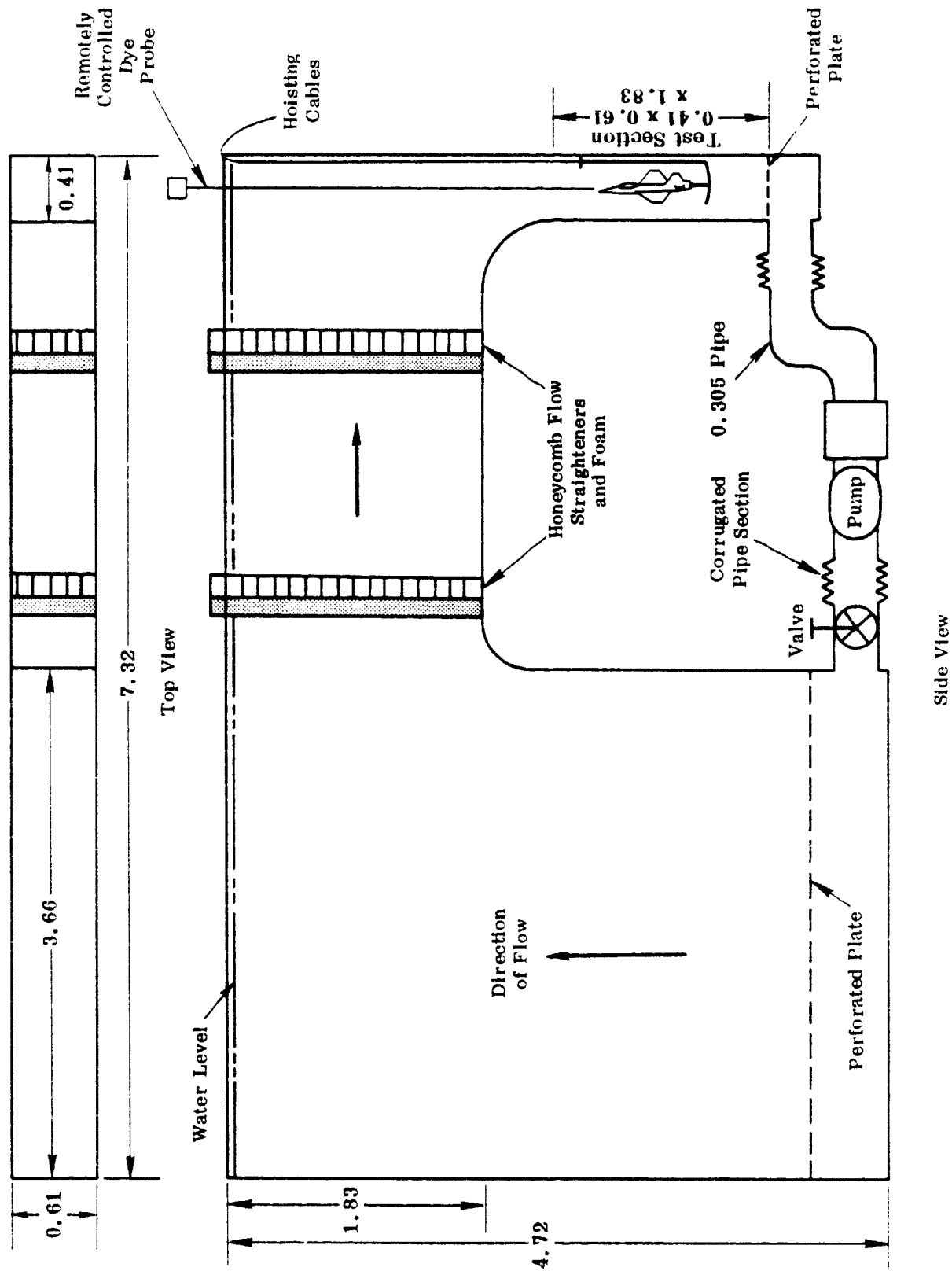


FIGURE 1. Northrop Diagnostic Water Tunnel (All Dimensions in m)

	<u>Facility (Method)</u>	<u>Reynolds No.</u>
○ Northrop 16 x 24 in.	Water Tunnel (Dye)	$2.0(10^4)$
● Northrop 6 x 6 in.	Water Tunnel (Dye)	$1.5(10^4)$
□ Wentz	Wind Tunnel (Schlieren)	10^6 (approx.)
◇ Poisson-Quinton & Erlich	Water Tank (Dye; alum- inum Particles)	$2(10^4)$ (approx.)
△ Chigier	Wind Tunnel (Laser anemometer)	$2(10^6)$ (approx.)
▽ Earnshaw and Lawford	Wind Tunnel (Tuft probe)	(10^6) (approx.)
▲ Hummel and Srinivasan	Wind Tunnel (Smoke)	(10^6) (approx.)
★ Lowson	Water Tunnel (Dye)	$3(10^4)$

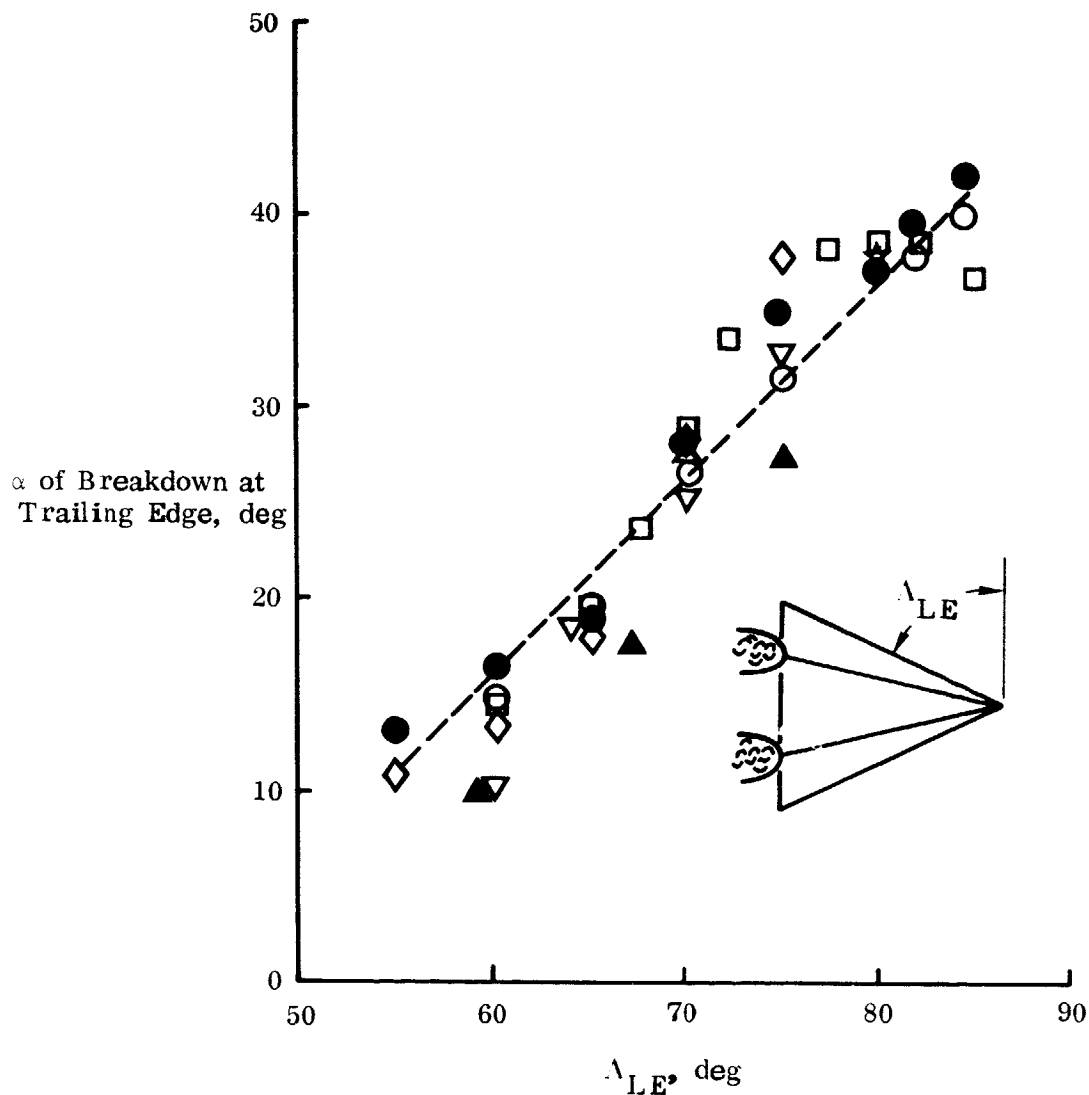


FIGURE 2. Effect of Leading-Edge Sweep on the Angle of Attack of Vortex Breakdown at the Trailing Edge of Delta Wings (Data from Reference 3)

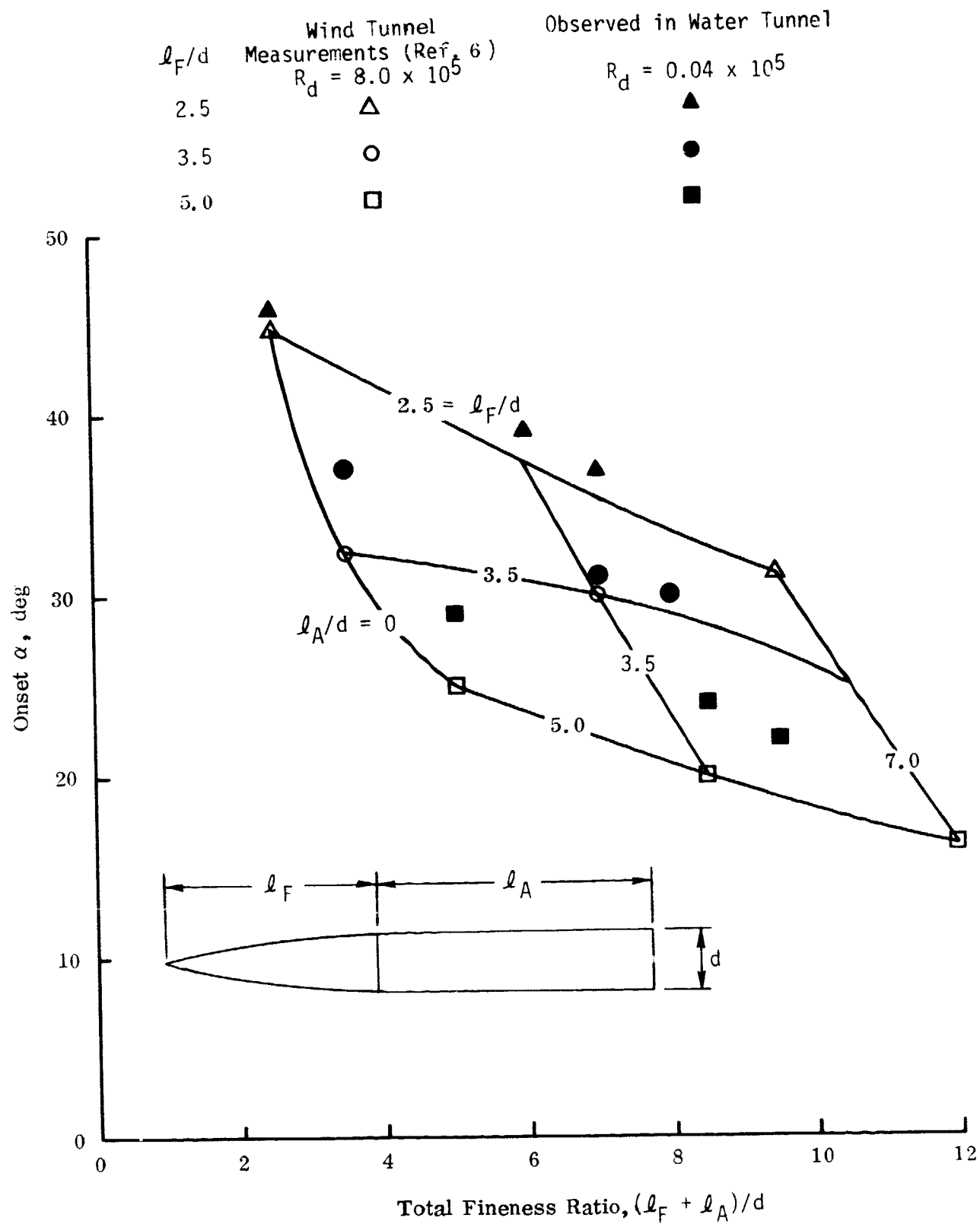


FIGURE 3. Onset of Vortex Asymmetry on Tangent Ogive - Cylinder Bodies

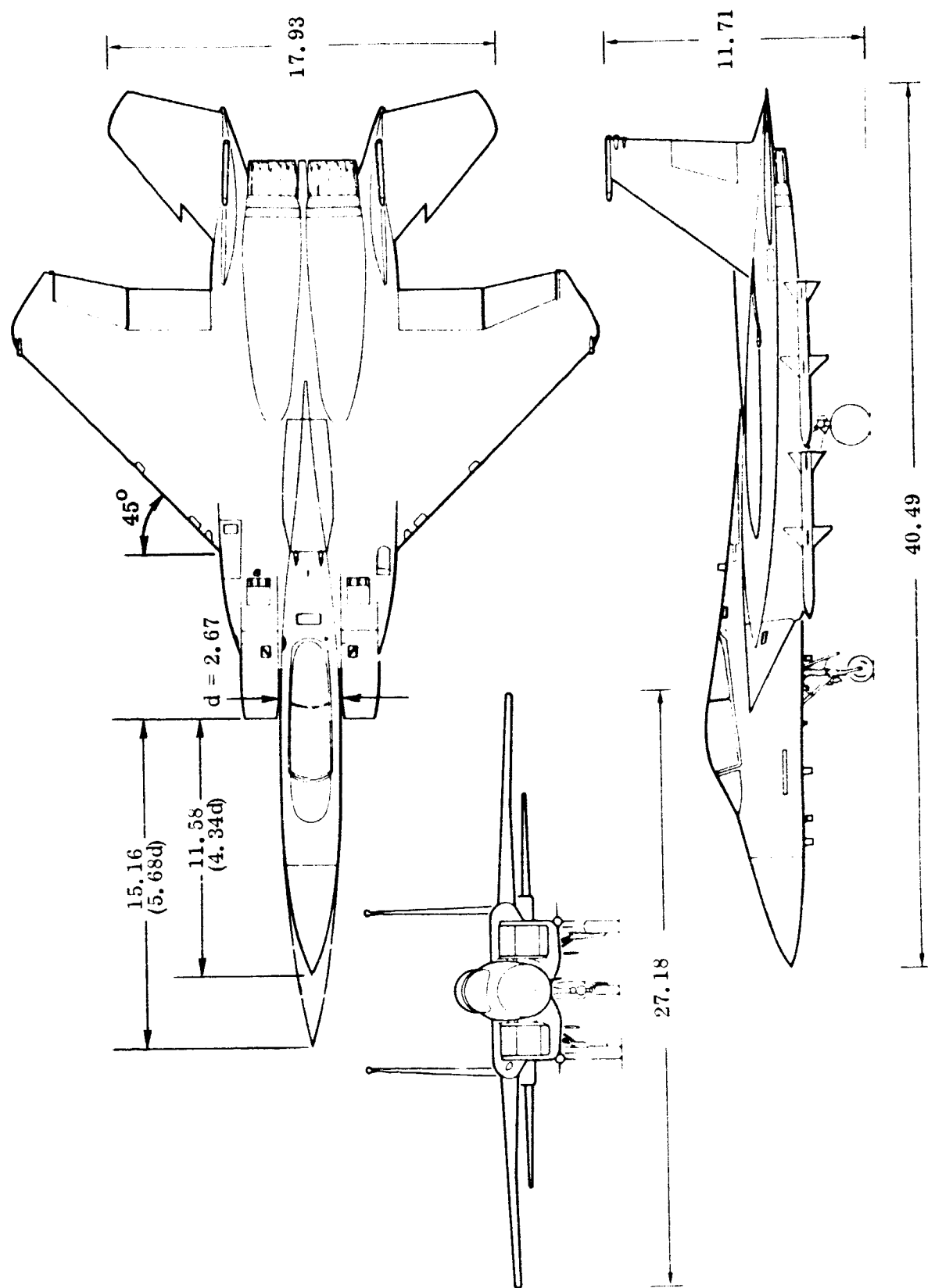


FIGURE 4. 1/48-Scale F-15 Three View Drawing (All Dimensions in cm)

ORIGINAL PAGE IS
OF POOR QUALITY

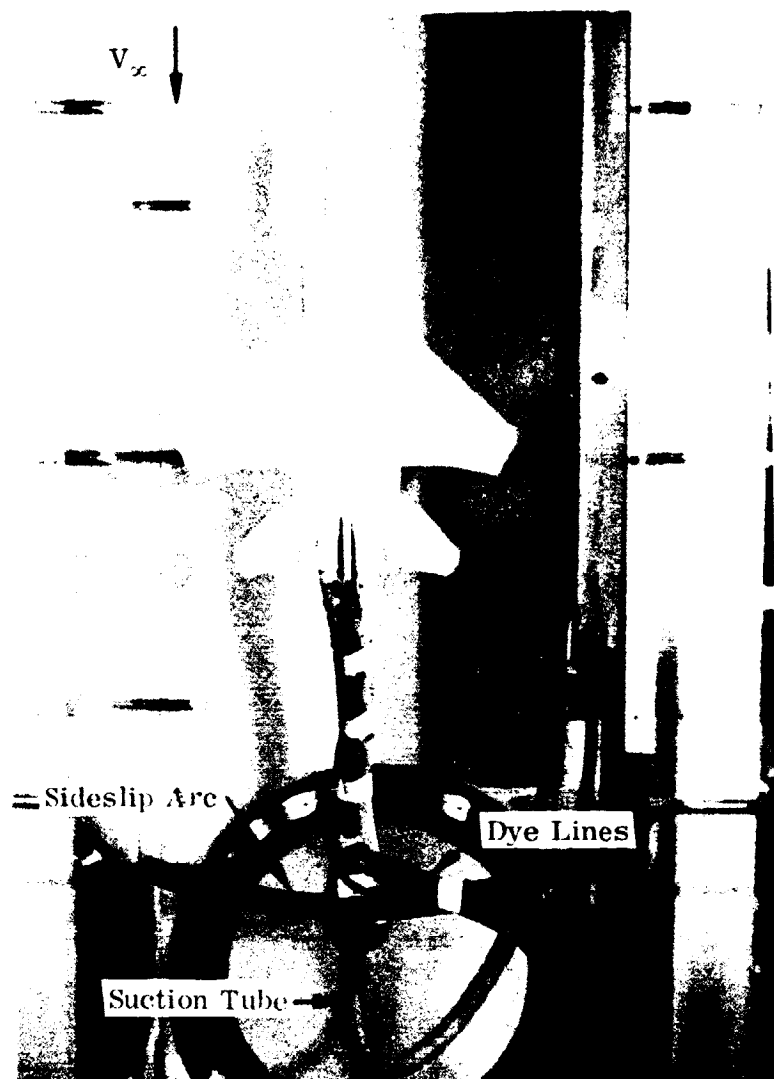


FIGURE 5. Model Installation

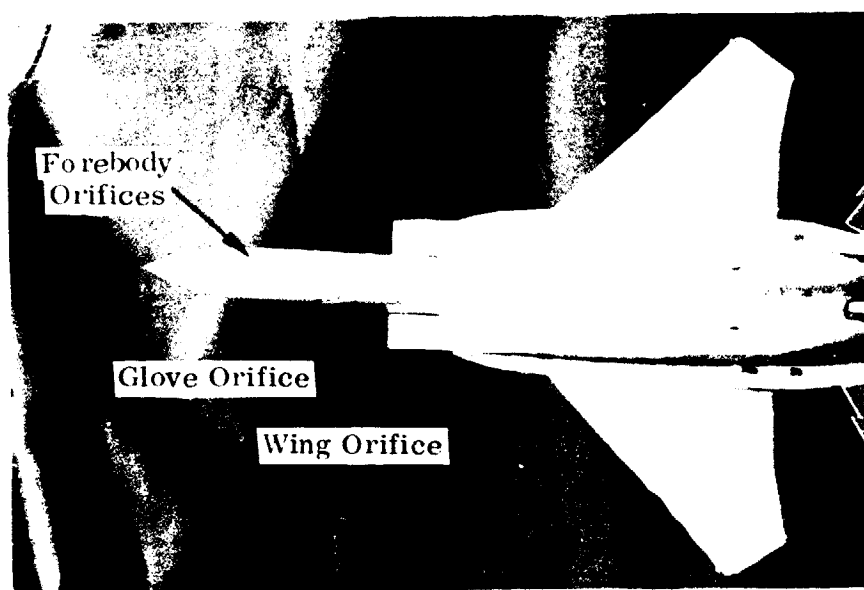


FIGURE 6. Dye Injection Orifices

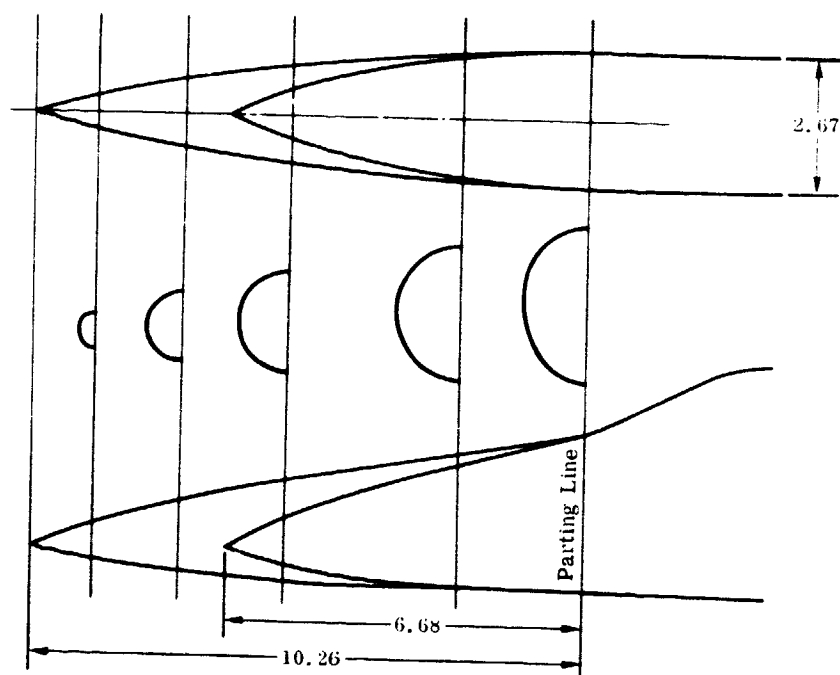


FIGURE 7. Production and Long Forebody

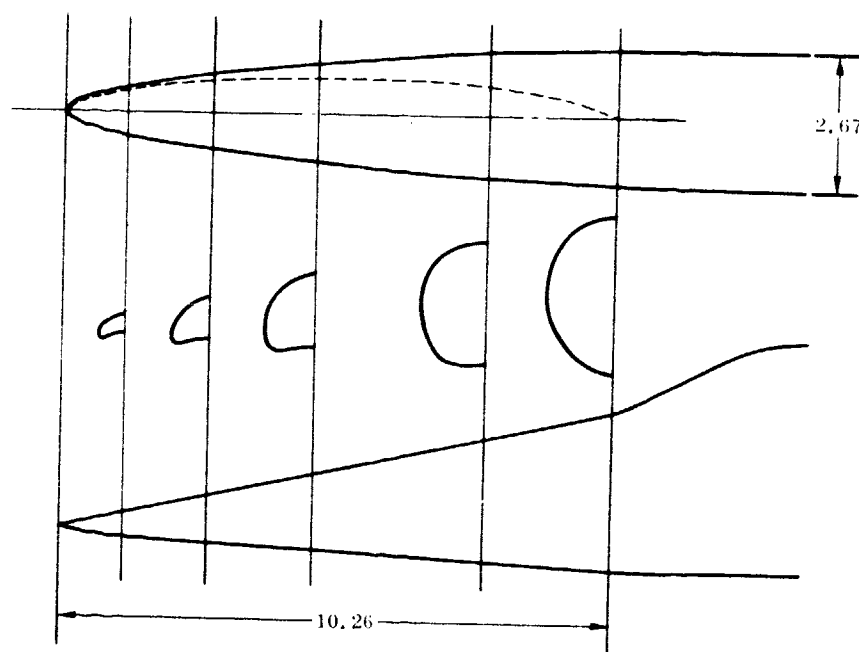


FIGURE 8. Cambered Forebody (All Dimensions in cm)

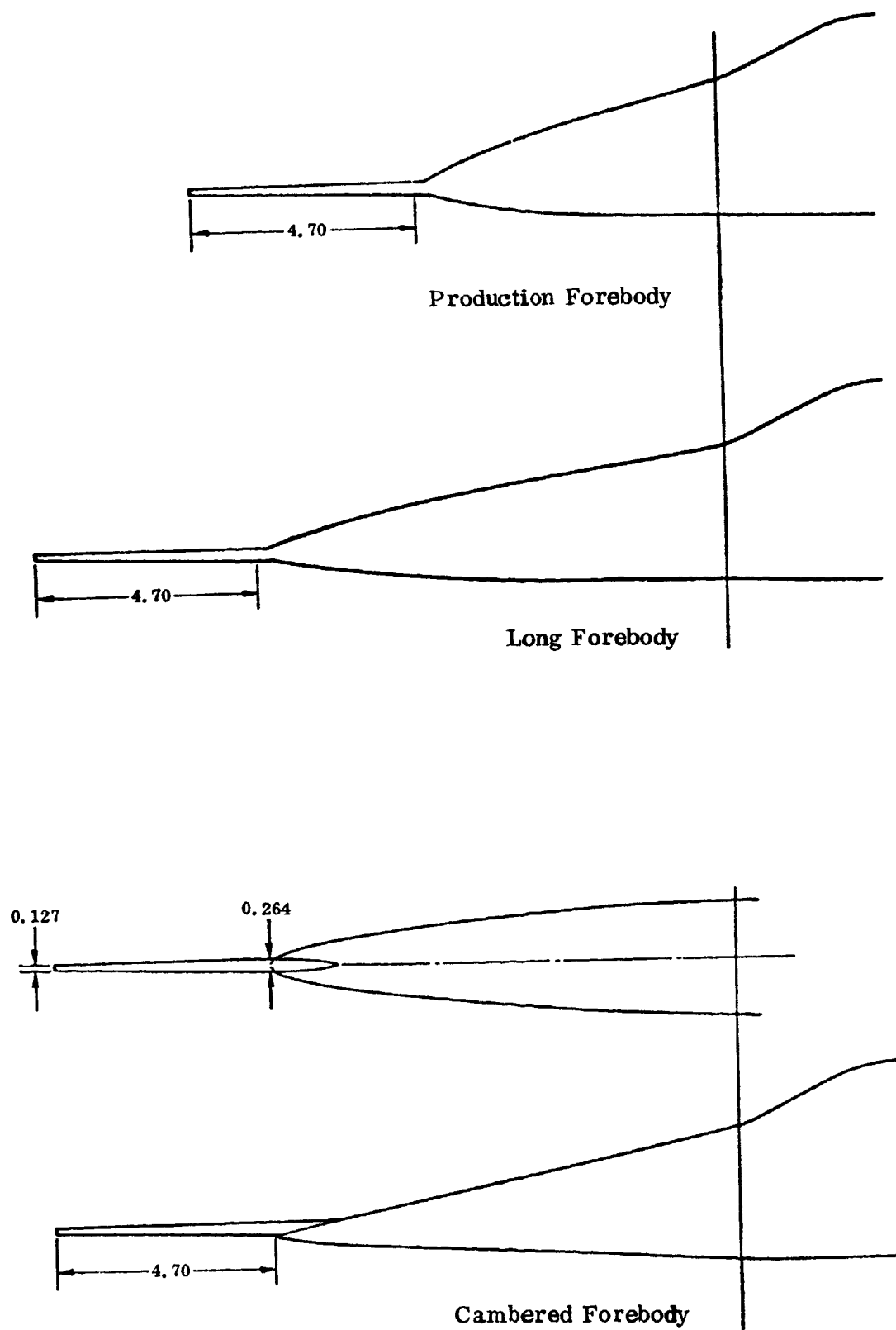


FIGURE 9. Nose Boom Installed on Forebodies (All Dimensions in cm)

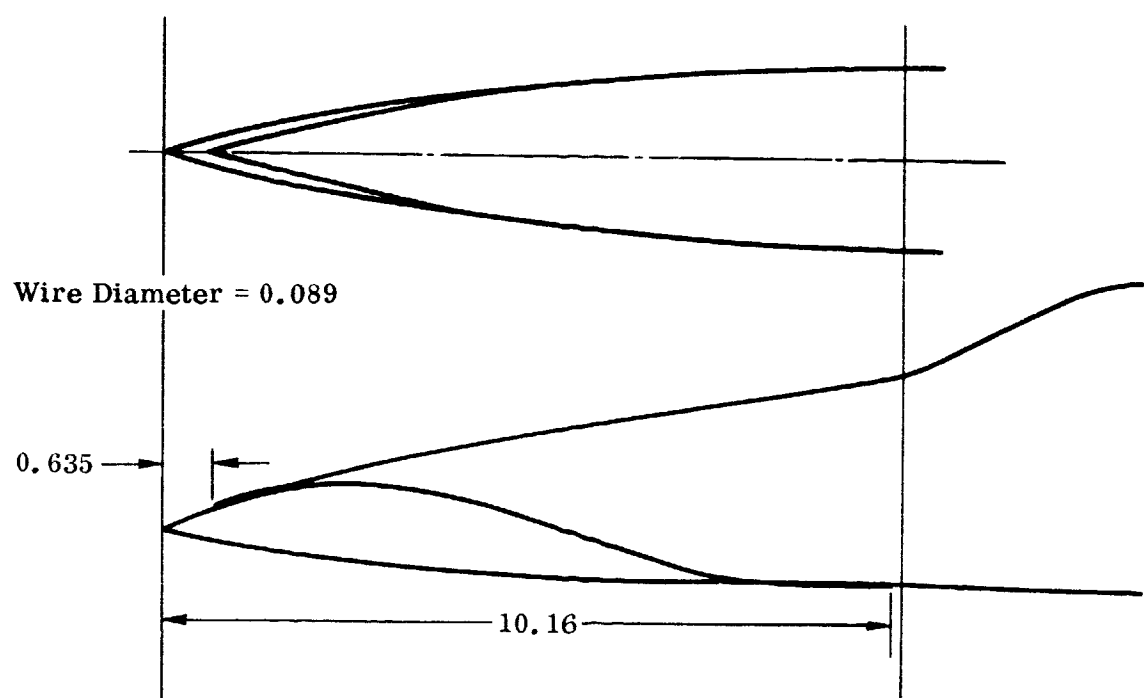


FIGURE 10. Helical Separation Trip (All Dimensions in cm)

Cowl Angle = 11°
 Military Power Setting
 Altitude = 35,000 Ft

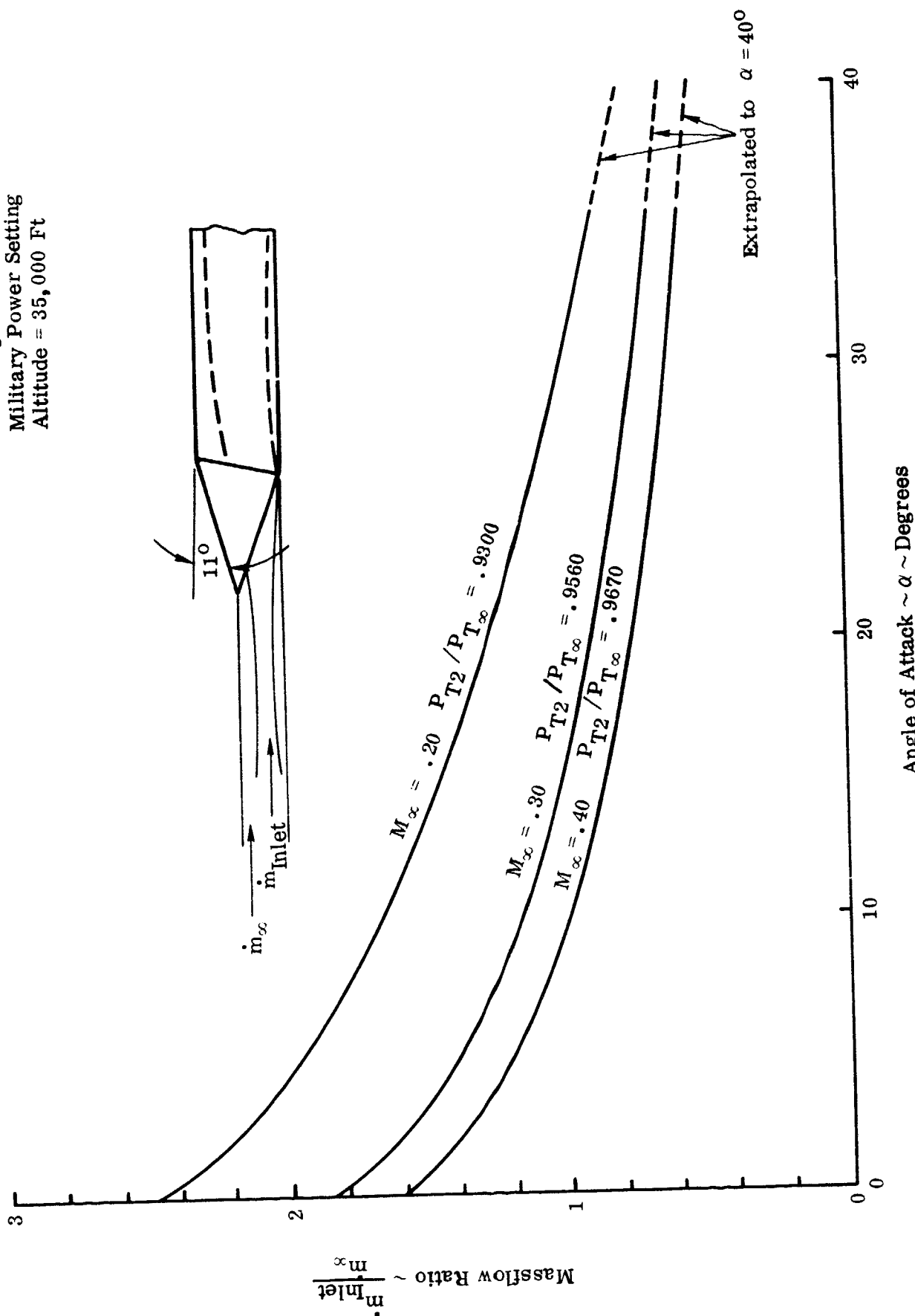
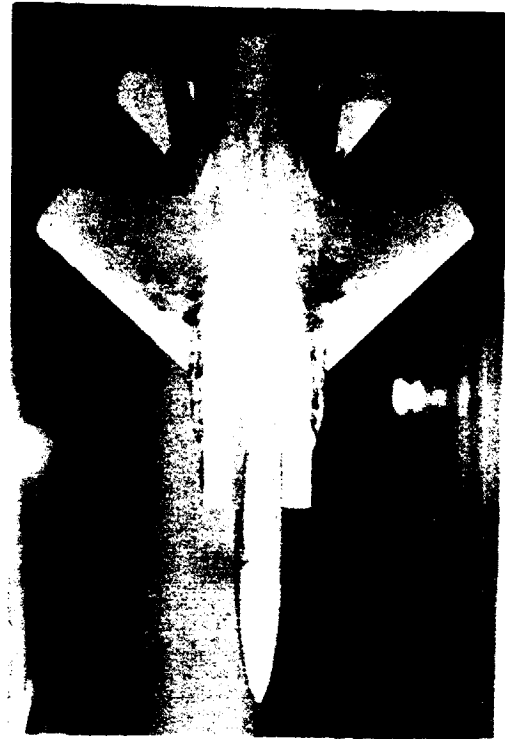


FIGURE 11. Theoretical Variation of F-15 Inlet Massflow Ratio with Freestream Angle of Attack

ORIGINAL PAGE IS
OF POOR QUALITY



$\alpha = 12^\circ$



$\alpha = 30^\circ$

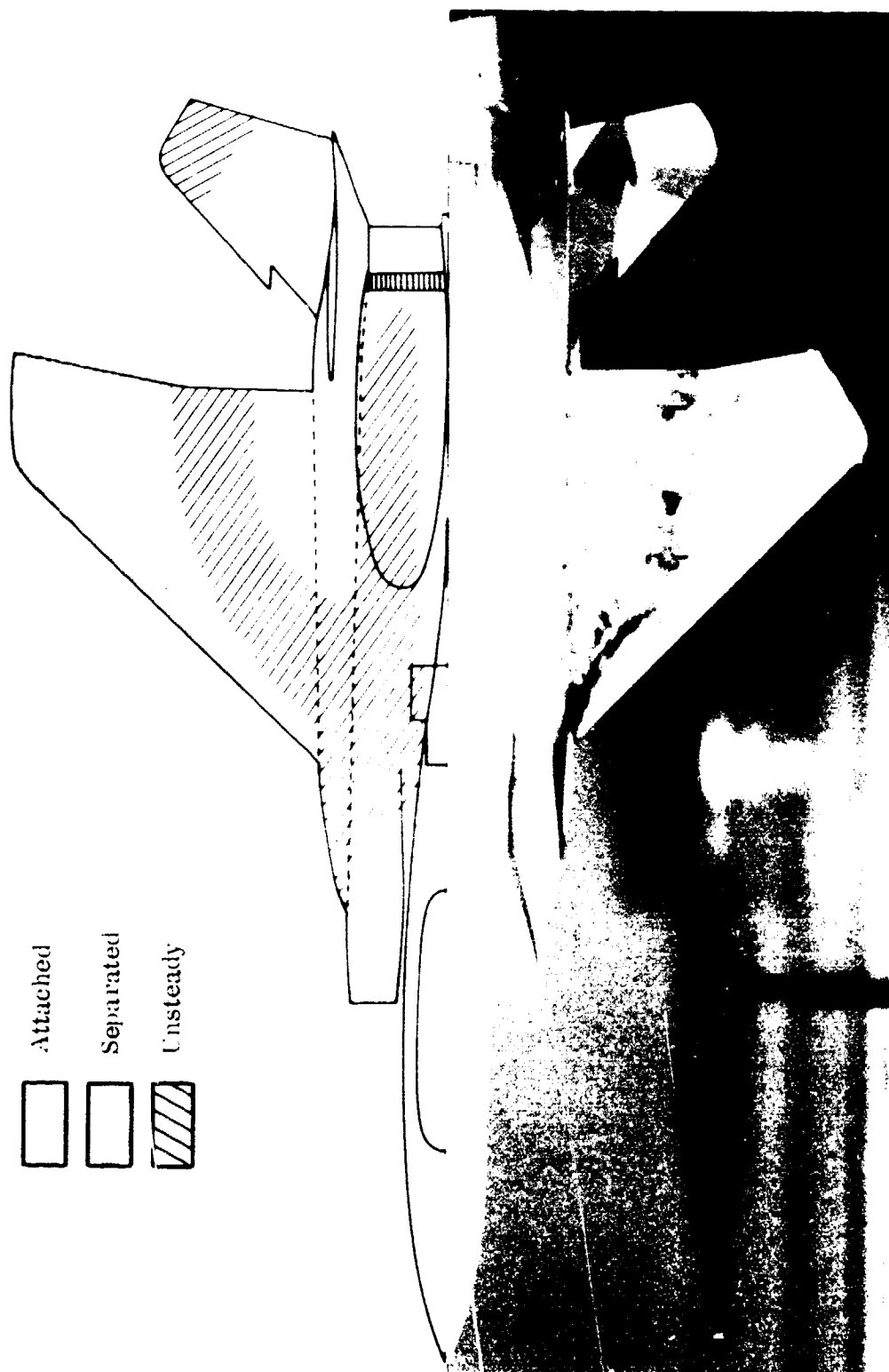


$\alpha = 5^\circ$



$\alpha = 18^\circ$

FIGURE 12. Baseline Configuration; Production Forebody, $(\dot{m}_1/\dot{m}_2)\alpha = 0$, 1.85 , $\delta_{II} = -29^\circ$, $\delta_I = 11^\circ$, $\beta = 0^\circ$



(a) $\alpha = 10^\circ$

FIGURE 13. Comparison of Tufts on Aircraft in Flight with Water Tunnel Flow Visualization; $\delta_I = 11^\circ$, $\beta = 0^\circ$

ORIGINAL PAGE IS
OF POOR QUALITY

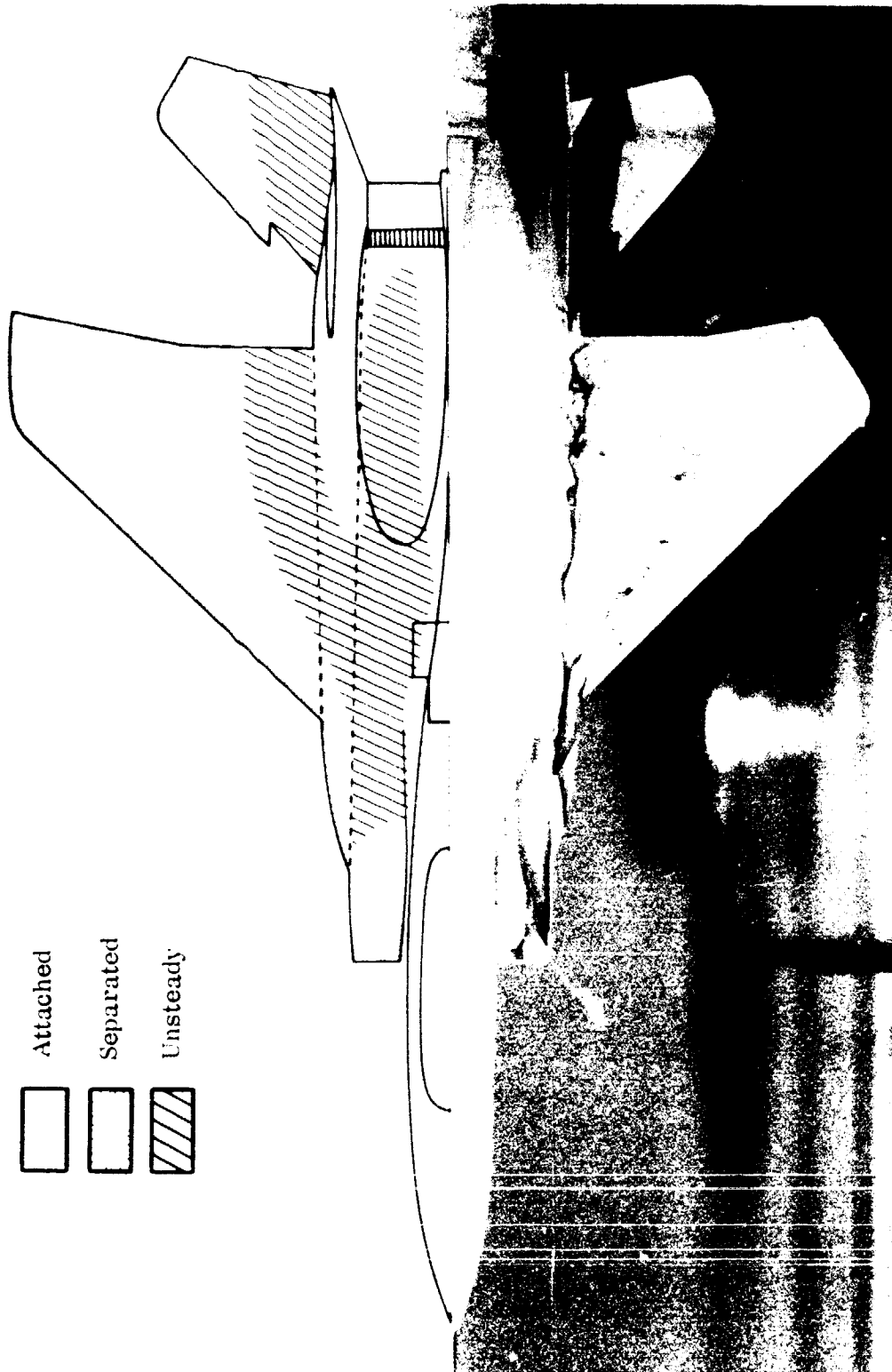


FIGURE 13. Continued

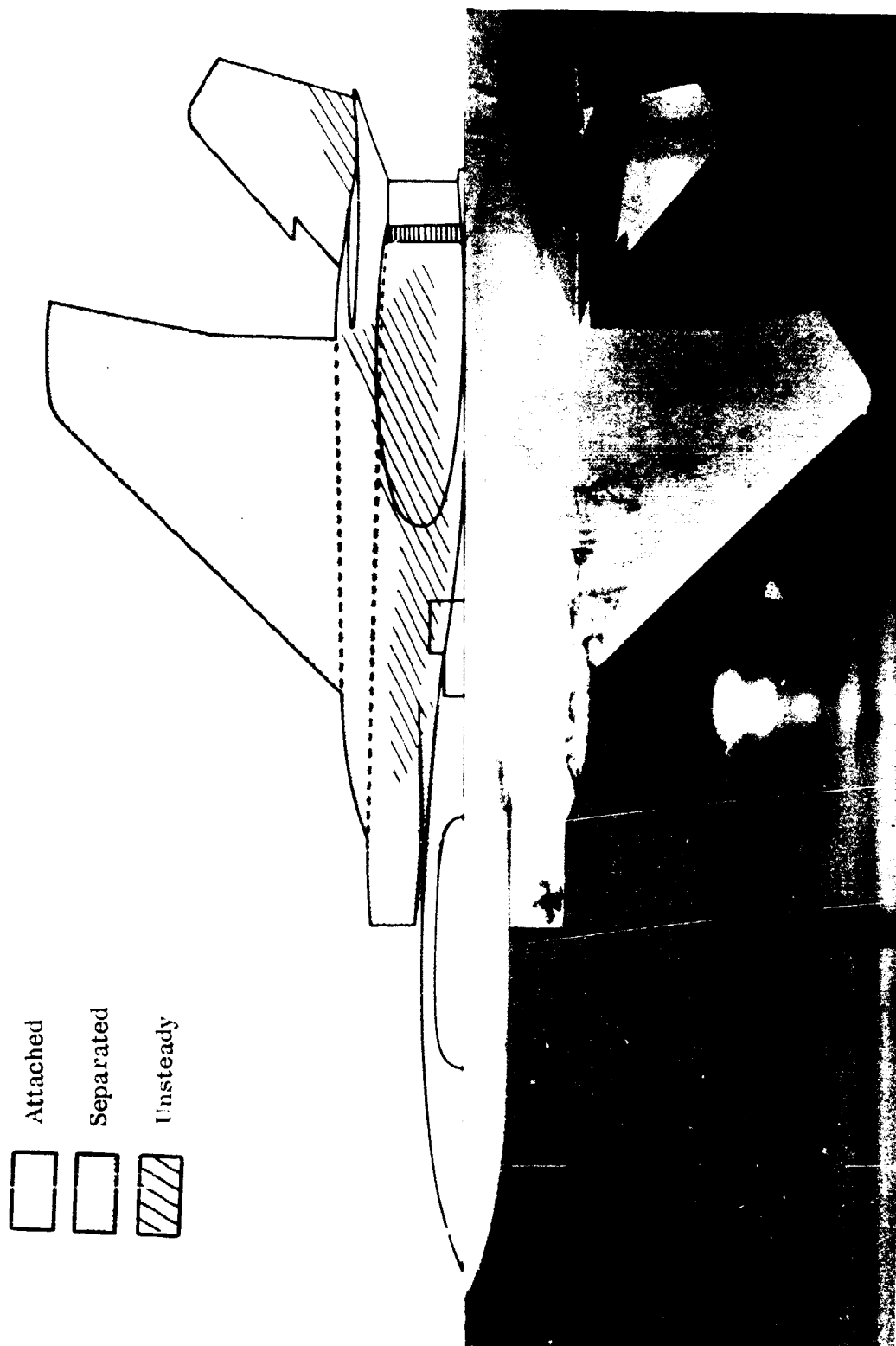


FIGURE 13. Continued

ORIGINAL PAGE IS
OF POOR QUALITY

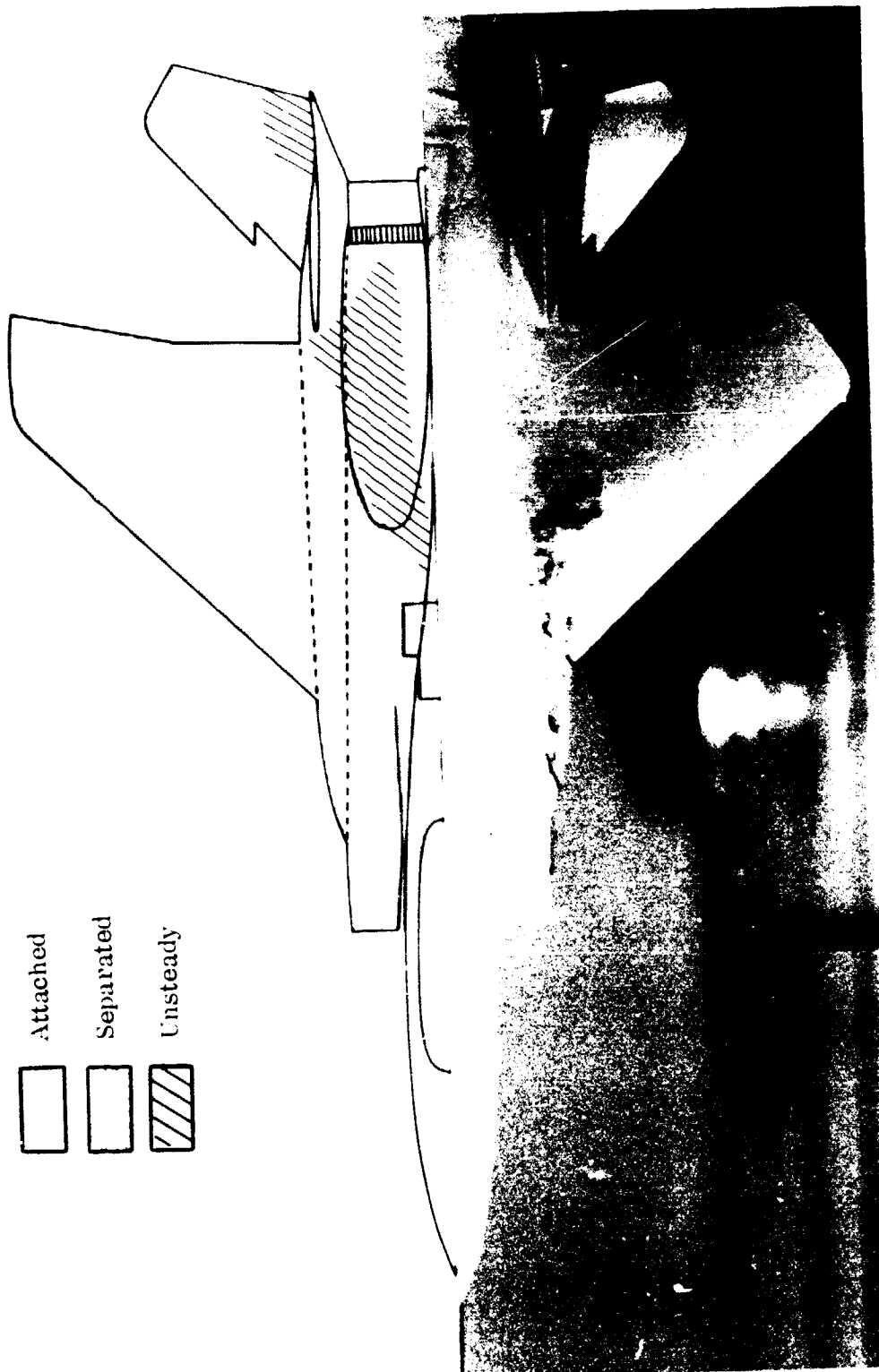


FIGURE 13. Concluded



$\alpha = 5^\circ$



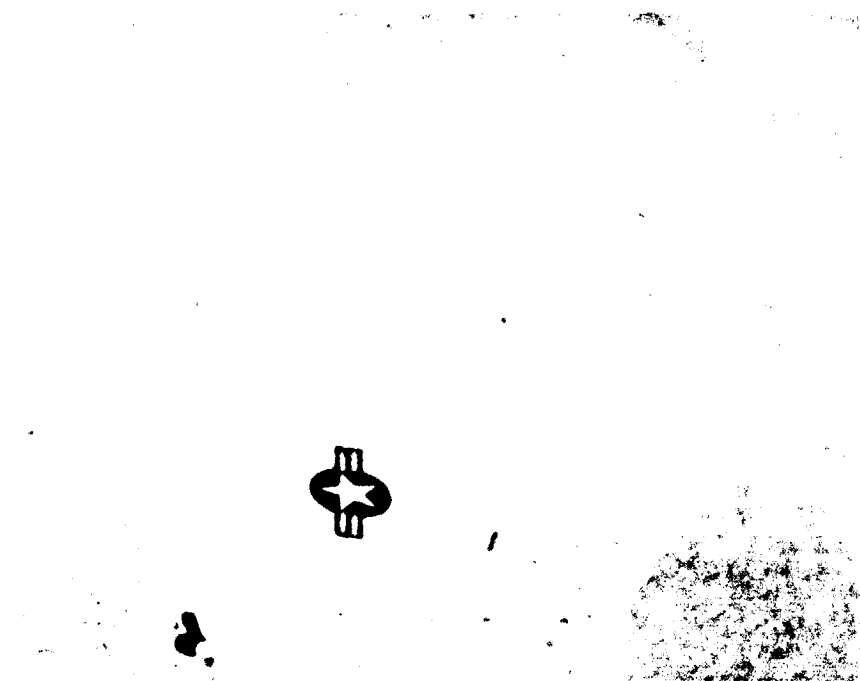
$\alpha = 12^\circ$

FIGURE 14. Tufts on the Aircraft in Flight at $M_\infty = 0.3$

ORIGINAL PAGE IS
OF POOR QUALITY

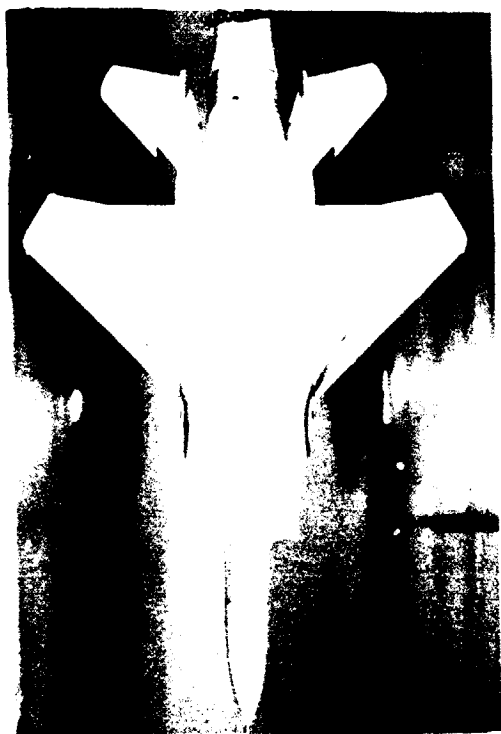


$\alpha = 18.5^\circ$



$\alpha = 24^\circ$

FIGURE 14. Concluded



$\alpha = 10^\circ$



$\alpha = 15^\circ$

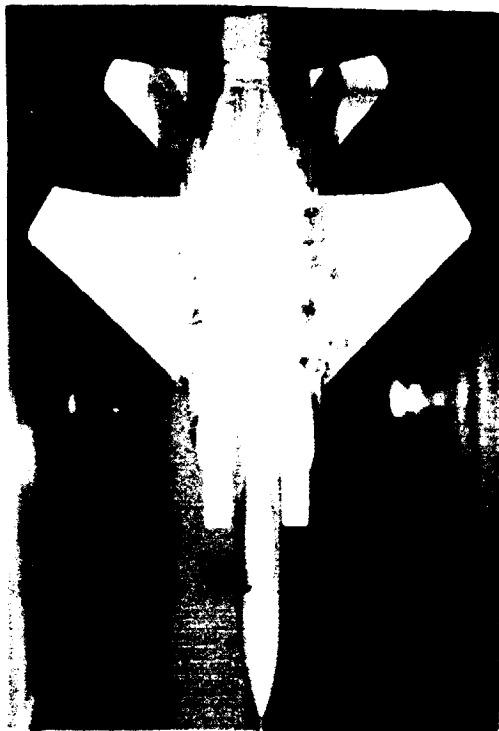


$\alpha = 20^\circ$

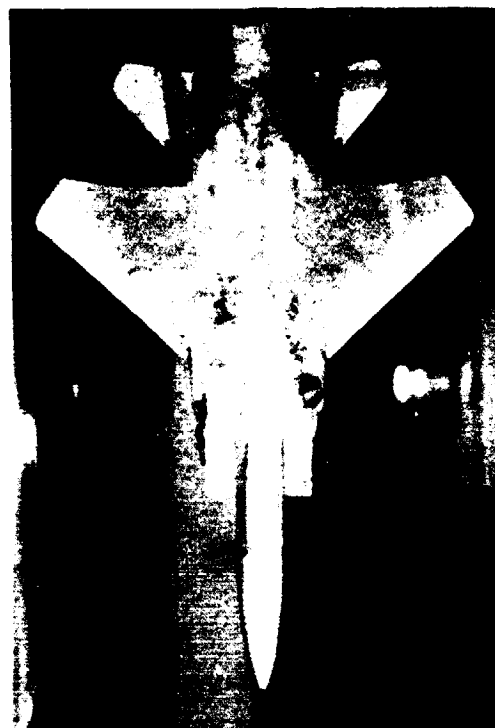


$\alpha = 30^\circ$

FIGURE 15. Effect of Inlet Flow on Wing Flow Field; Production Forebody,
 $(\dot{m}_I / \dot{m}_\infty)_{\alpha=0} = -2.48, \delta_{II} = -29^\circ, \delta_I = 11^\circ, \beta = 0^\circ$



$\alpha = 12^\circ$



$\alpha = 25^\circ$



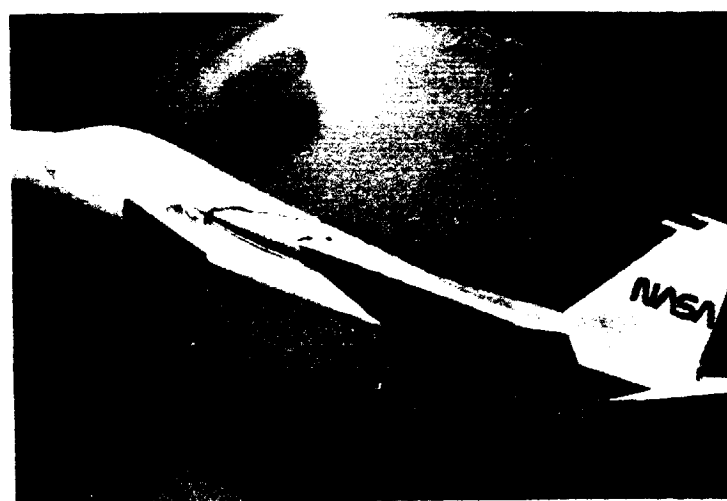
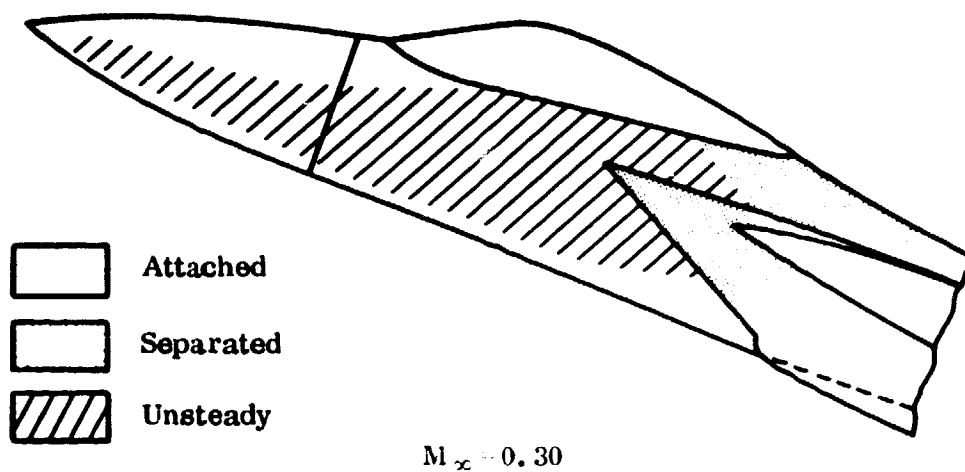
$\alpha = 10^\circ$



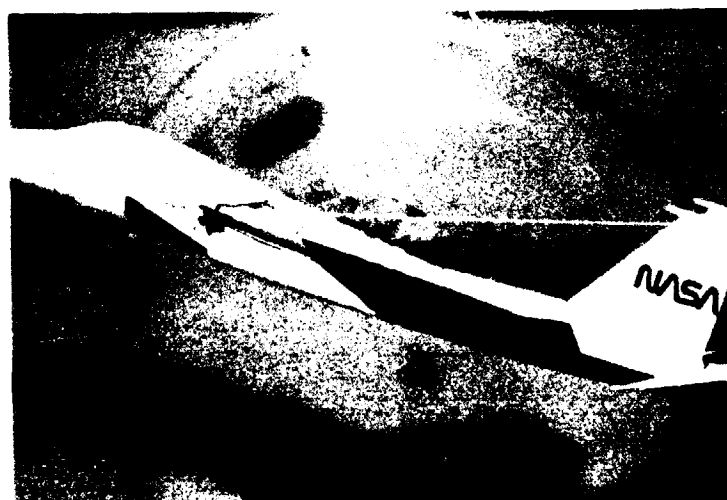
$\alpha = 15^\circ$

FIGURE 16. Effect of Inlet Flow on Wing Flow Field; Production Forebody,

$(\dot{m}_I / \dot{m}_\infty)_{\alpha=0} = 0, \delta_H = -29^\circ, \delta_I = 11^\circ, \beta = 0^\circ$



$$(\dot{m}_I / \dot{m}_\infty)_{\alpha=0} = 1.85$$

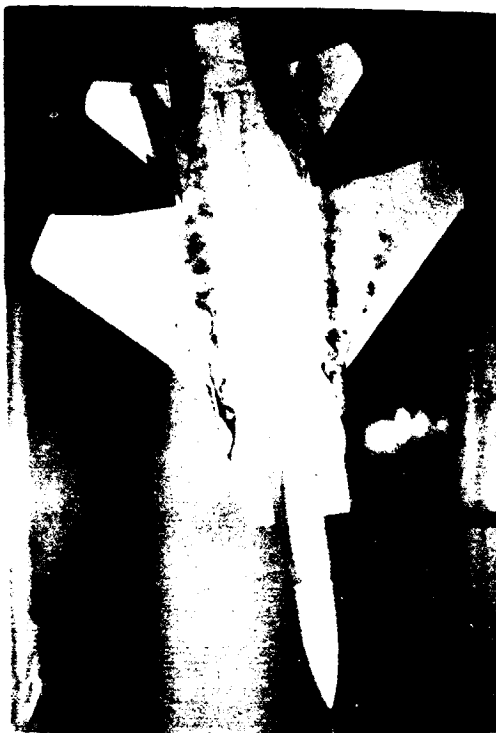


$$(\dot{m}_I / \dot{m}_\infty)_{\alpha=0} = 0$$

FIGURE 17. Inlet Side Wall; $\alpha = 20^\circ$, $\beta = 0^\circ$, $\delta_I = 11^\circ$



$\alpha = 10^\circ$



$\alpha = 15^\circ$



$\alpha = 20^\circ$



$\alpha = 25^\circ$

FIGURE 1. Effect of Sideslip on Wing Flow Field; Production Forebody,
 $(\dot{m}_I / \dot{m}_\infty) \alpha = 0, 1.85, \delta_{II} = -29^\circ, \delta_I = 11^\circ, \beta = 10^\circ$

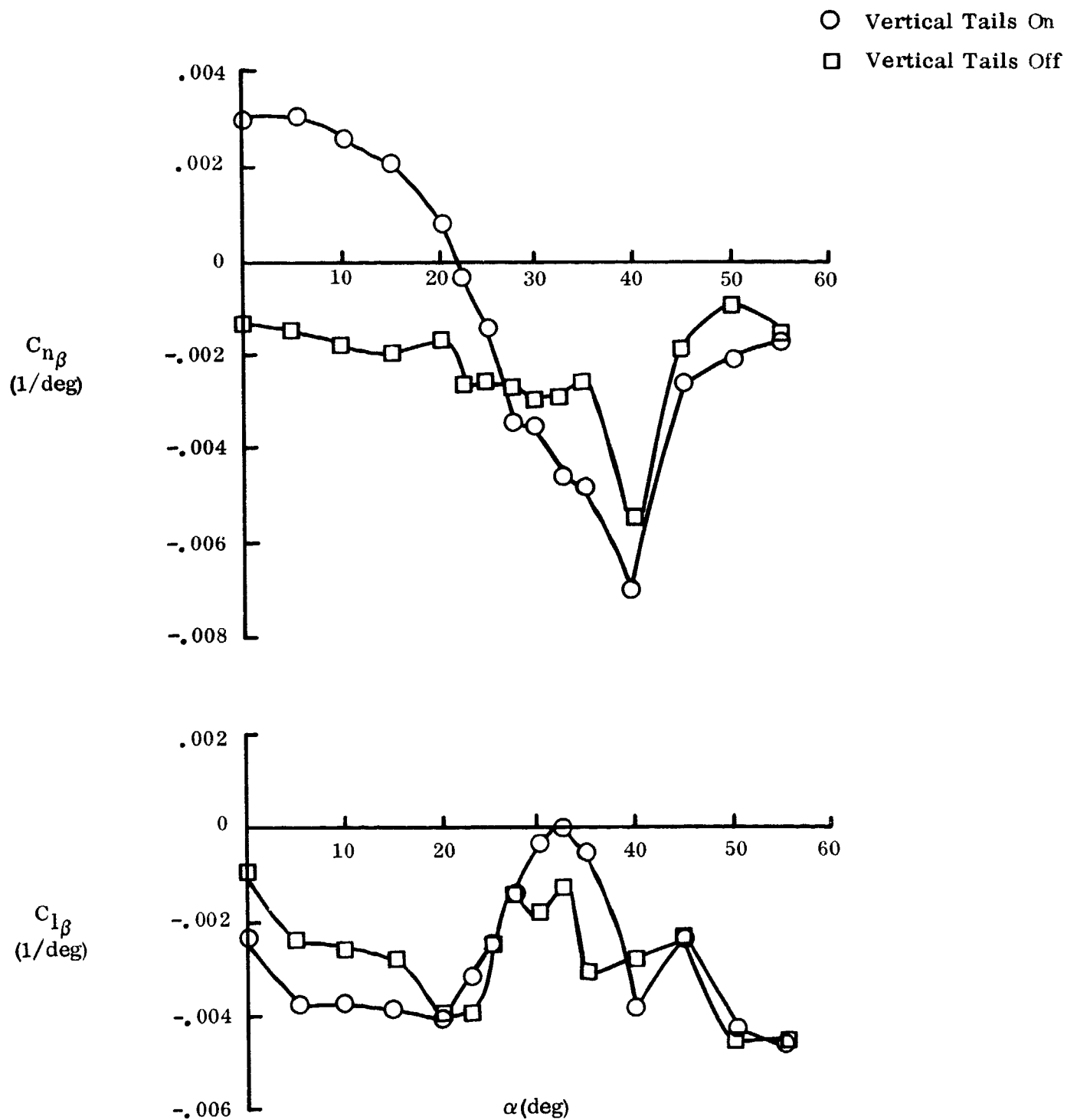
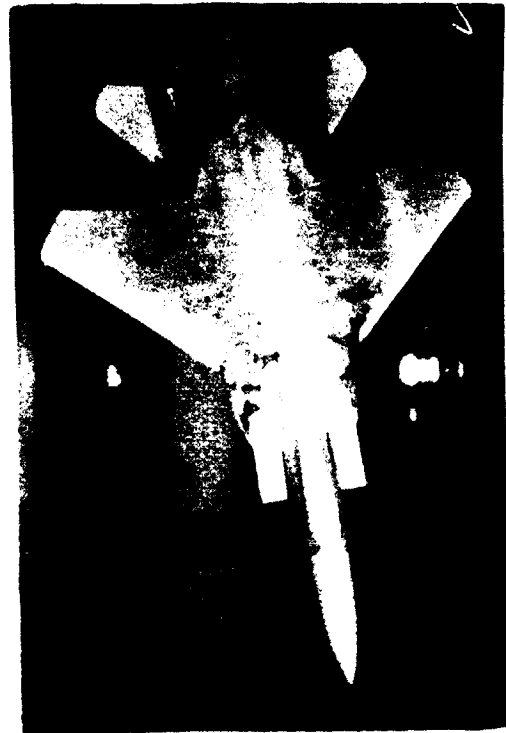


FIGURE 19. Effect of Vertical Tails on Lateral-Directional Stability;
Long Forebody, $\delta_H = 0^\circ$, $\delta_I = 12^\circ$



$\alpha = 15^\circ$



$\alpha = 25^\circ$

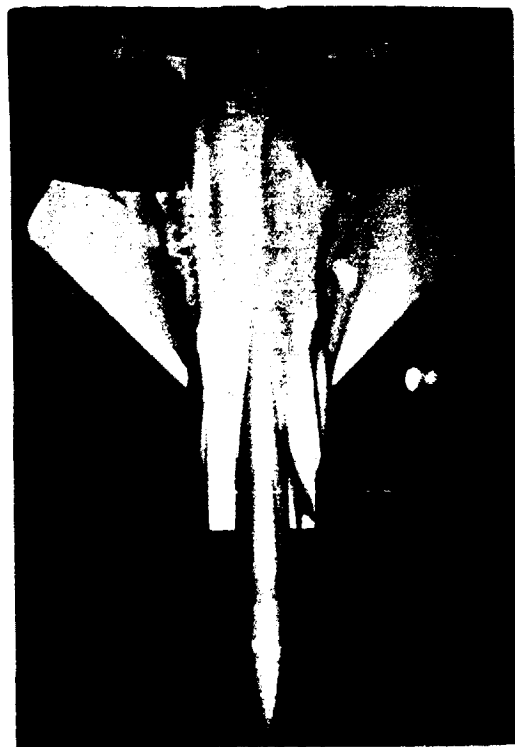


$\alpha = 10^\circ$

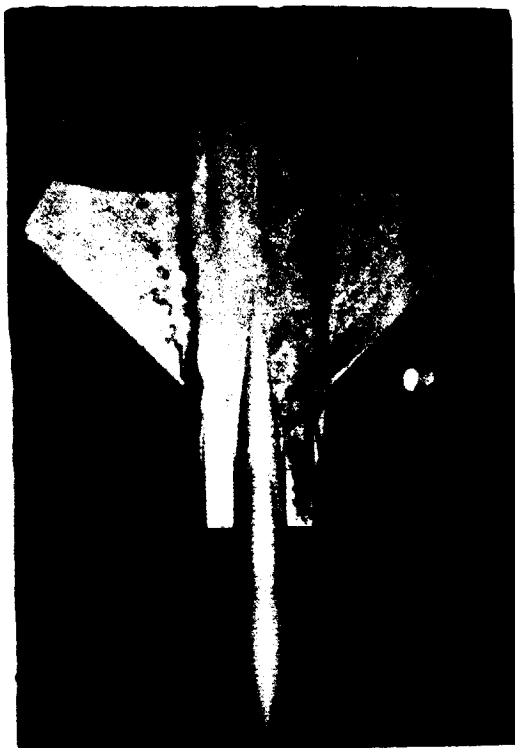


$\alpha = 20^\circ$

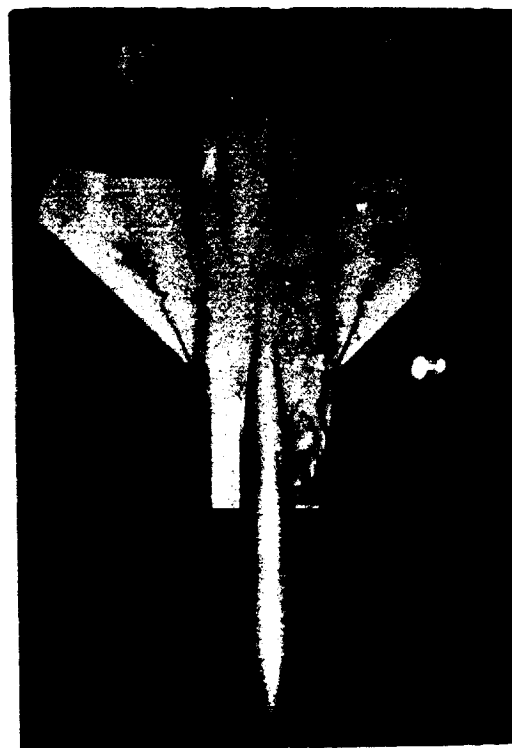
FIGURE 20. Effect of Sideslip on Wing Flow Field; Production Forebody,
 $(\dot{m}_I / \dot{m}_\infty)_{\alpha=0} = 0$, $\delta_H = -29^\circ$, $\delta_I = 11^\circ$, $\beta = 10^\circ$



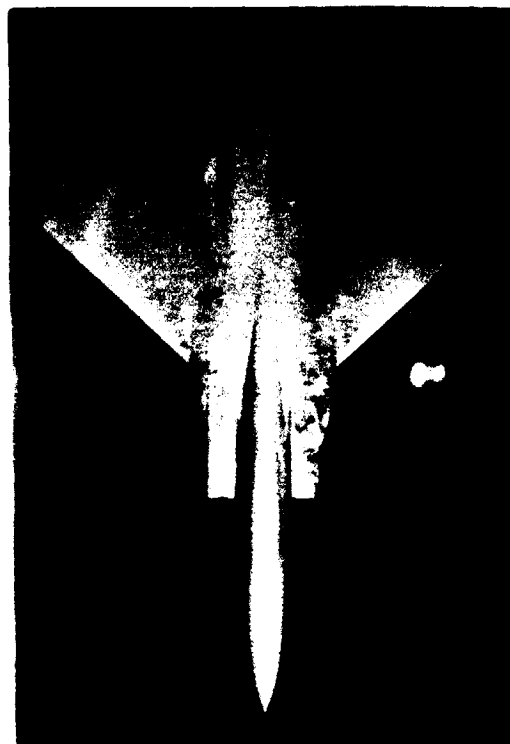
$\alpha = 7^\circ$



$\alpha = 10^\circ$



$\alpha = 15^\circ$

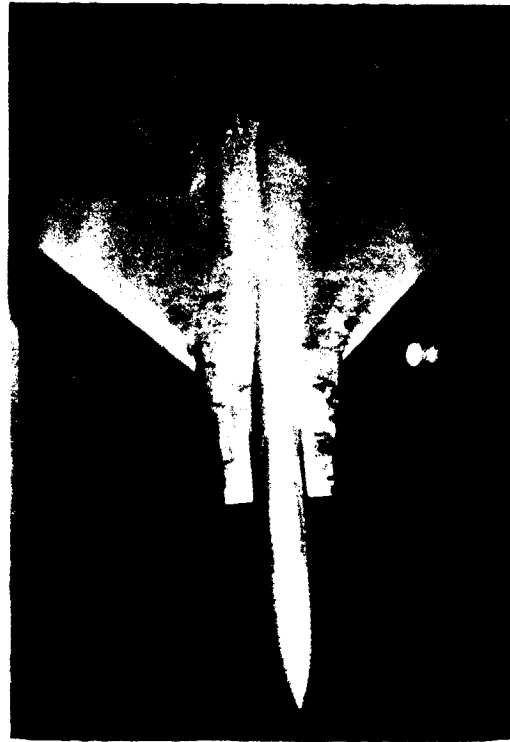


$\alpha = 25^\circ$

FIGURE 21. Effect of Inlet Deflection Angle on Wing Flow Field; Production Forebody,
 $(\dot{m}_I / \dot{m}_\infty) \alpha = 0, 1.85, \delta_H = -29^\circ, \delta_I = 0^\circ, \beta = 0^\circ$



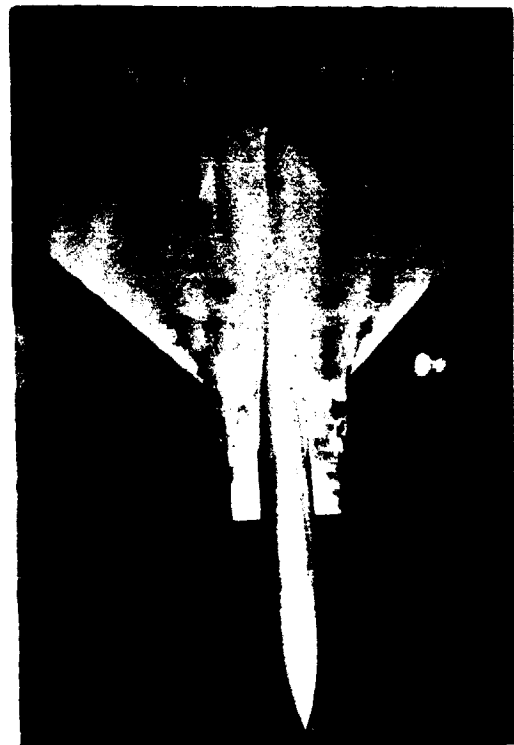
$\alpha = 15^\circ$



$\alpha = 25^\circ$



$\alpha = 10^\circ$



$\alpha = 20^\circ$

FIGURE 22. Effect of Inlet Deflection Angle on Wing Flow Field; Production Forebody,
($\dot{m}_I / \dot{m}_\infty$) $\alpha = 0 = 1.85$, $\delta_{II} = -29^\circ$, $\delta_I = 0^\circ$, $\beta = 5^\circ$

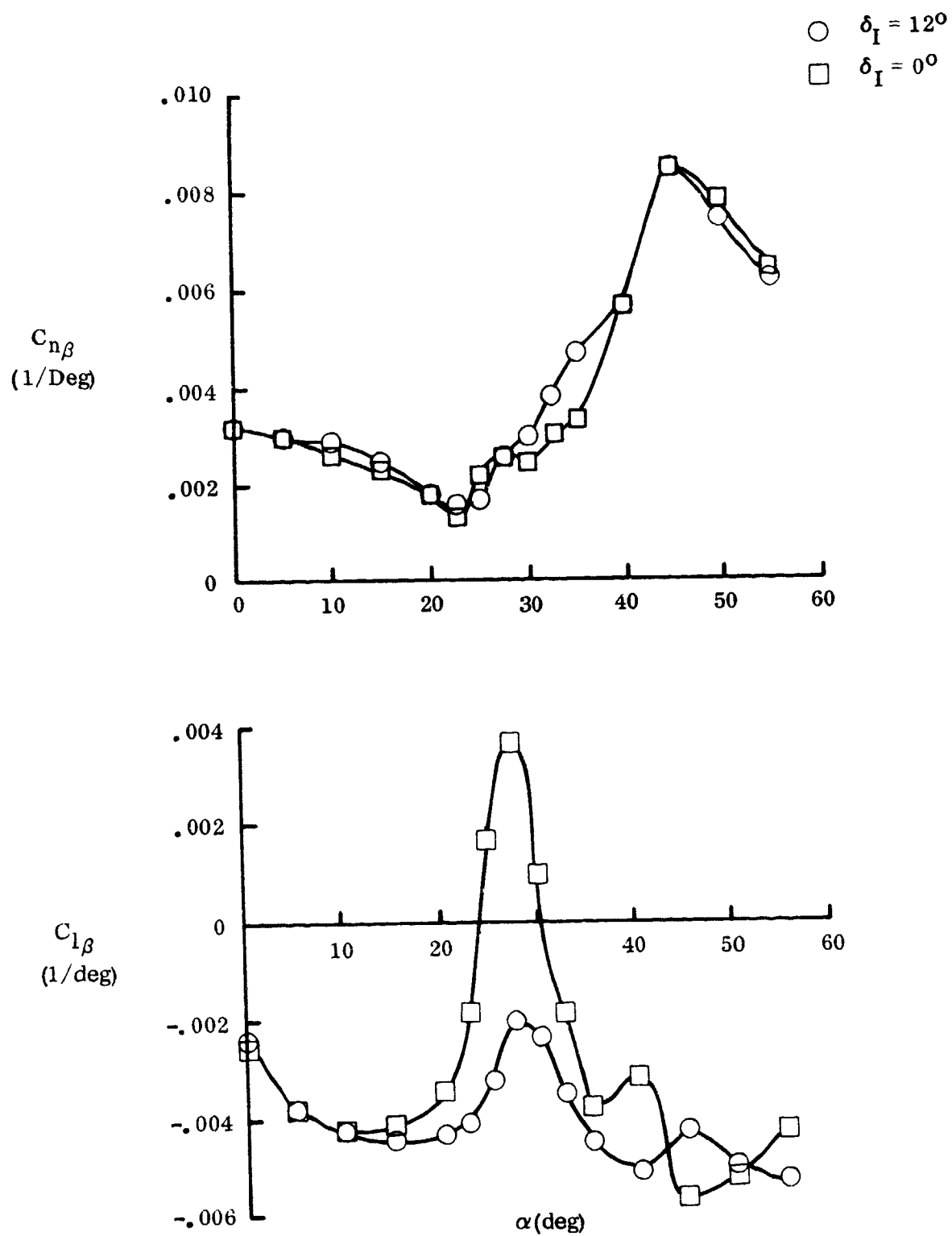
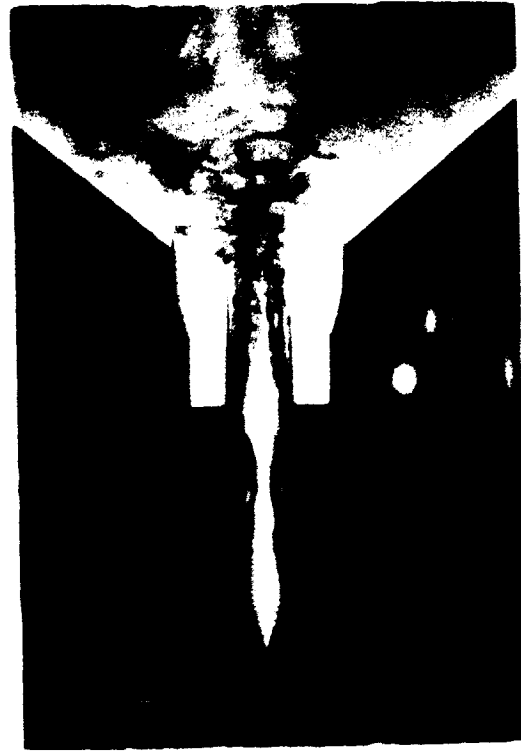


FIGURE 23. Effect of Inlet Deflection Angle on Lateral-Directional Stability; Cambered Forebody, $\delta_H = 0^\circ$

ORIGINAL PAGE IS
OF POOR QUALITY



$\alpha = 20^\circ$



$\alpha = 30^\circ$



$\alpha = 20^\circ$



$\alpha = 30^\circ$

FIGURE 24. Production Forebody Flow Field; $(\dot{m}_1/\dot{m}_\infty)\alpha = 0^\circ, \delta_H = -29^\circ, \delta_I = 11^\circ, \beta = 0^\circ$

ORIGINAL PAGE IS
OF POOR QUALITY



$\alpha = 40^\circ$



$\alpha = 55^\circ$



$\alpha = 40^\circ$

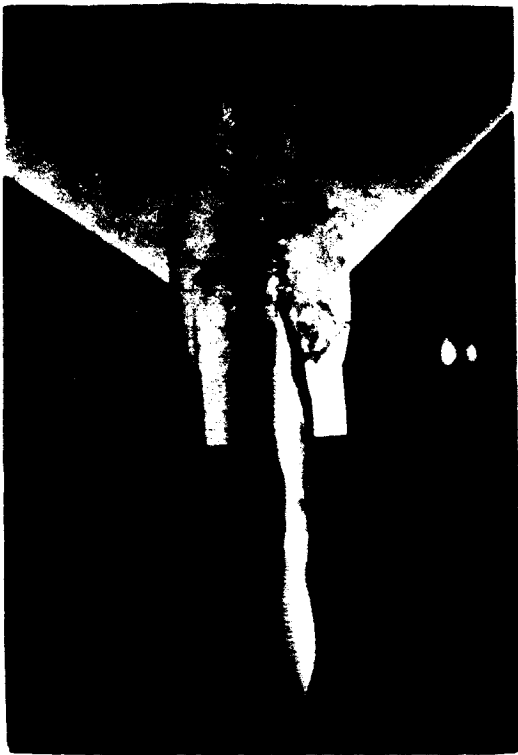


$\alpha = 55^\circ$

FIGURE 24. Concluded



$\alpha = 30^\circ$



$\alpha = 30^\circ$



$\alpha = 50^\circ$



$\alpha = 50^\circ$

FIGURE 25. Production Forebody Flow Field; $(\dot{m}_I/\dot{m}_\infty)$ $\alpha = 0, \delta_{II} = -29^\circ, \delta_I = 11^\circ, \beta = 5^\circ$

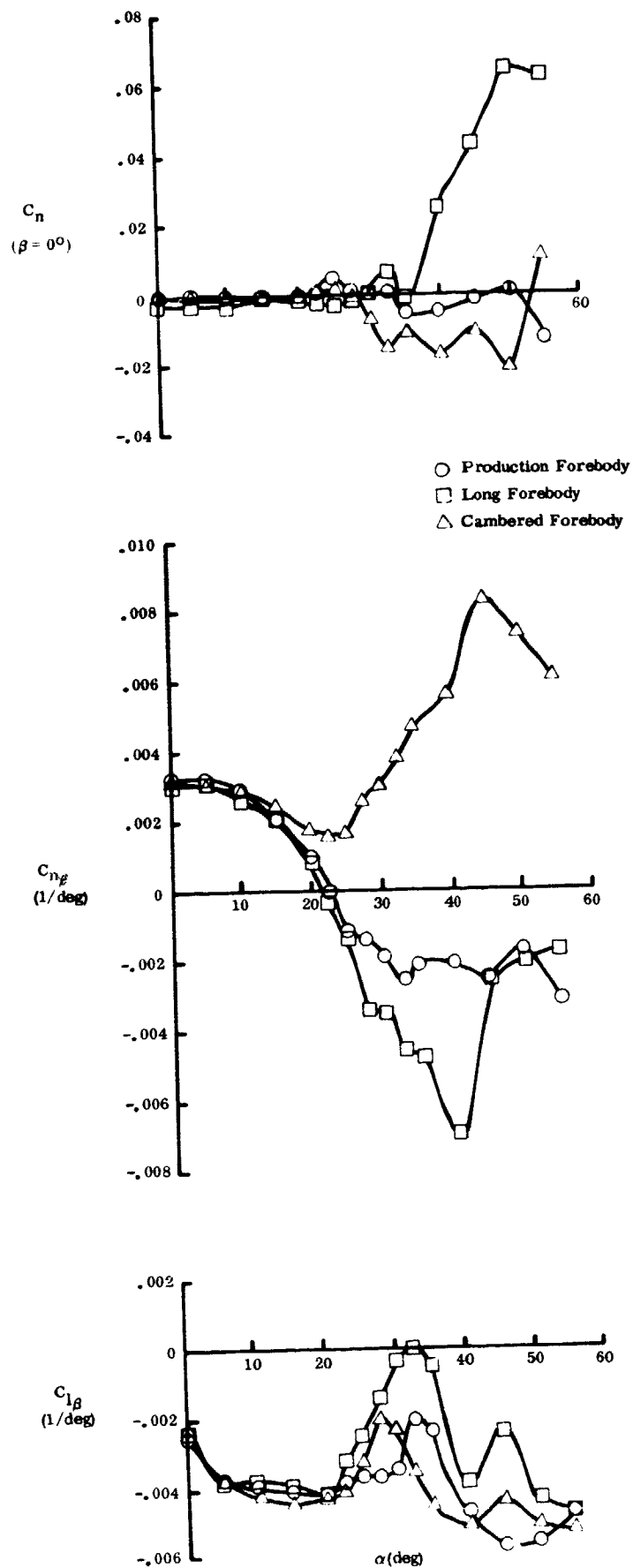


FIGURE 26. Effect of Forebody Fineness Ratio and Cross Section;
 $\delta_H = 0^\circ$, $\delta_I = 12^\circ$



$\alpha = 20^\circ, (\dot{m}_1/\dot{m}_2)\alpha = 0$



$\alpha = 40^\circ, (\dot{m}_1/\dot{m}_2)\alpha = 0$

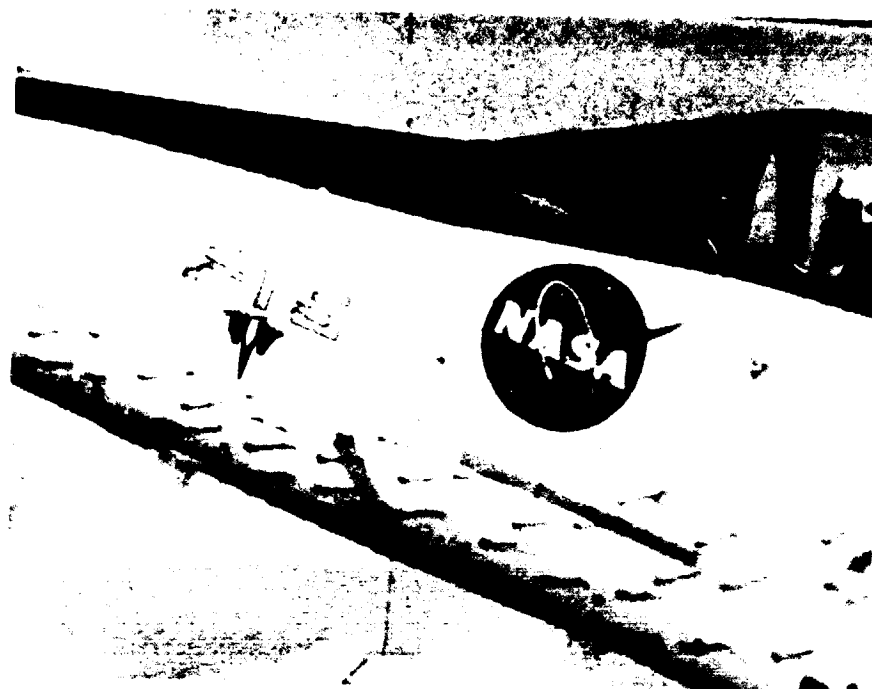


$\alpha = 20^\circ, (\dot{m}_1/\dot{m}_2)\alpha = 1.85$



$\alpha = 40^\circ, (\dot{m}_1/\dot{m}_2)\alpha = 1.85$

FIGURE 27. Effect of Inlet Flow on Production Forebody; $\delta_{II} = -29^\circ$, $\delta_I = 11^\circ$, $\beta = 0^\circ$



Full-Scale in Flight



1/48-Scale in Water Tunnel

FIGURE 28. Production Forebody Flow Field in Flight and
Water Tunnel: $\alpha = 20^\circ$, $\beta = 0^\circ$, $\delta_I = 11^\circ$



$\alpha = 25^\circ$



$\alpha = 35^\circ$



$\alpha = 25^\circ$



$\alpha = 35^\circ$

FIGURE 29. Long Forebody Flow Field; $(\dot{m}_1/\dot{m}_\infty)_{\alpha=0^\circ}, \delta_{II} = -29^\circ, \delta_I = 11^\circ, \beta = 0^\circ$



$\alpha = 40^\circ$



$\alpha = 50^\circ$



$\alpha = 40^\circ$



$\alpha = 50^\circ$

FIGURE 29. Concluded

ORIGINAL PAGE IS
OF PCOR QUALITY



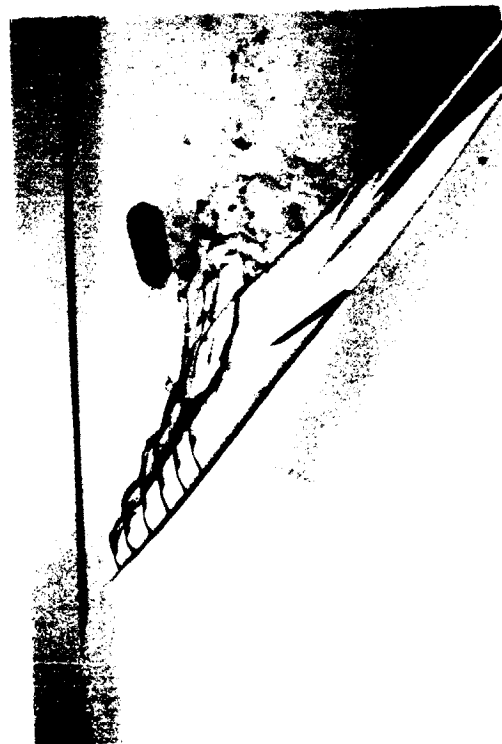
$\alpha = 35^\circ$



$\alpha = 40^\circ$



$\alpha = 35^\circ$



$\alpha = 40^\circ$

FIGURE 30. Long Forebody Flow Field; $(\dot{m}_I / \dot{m}_\infty)_{\alpha=0} = 0$, $\delta_H = -29^\circ$, $\delta_I = 11^\circ$, $\beta = 5^\circ$



$\alpha = 45^\circ$



$\alpha = 50^\circ$



$\alpha = 45^\circ$



$\alpha = 50^\circ$

FIGURE 30. Concluded

ORIGINAL PAGE IS
OF POOR QUALITY



$\alpha = 40^\circ$



$\alpha = 50^\circ$

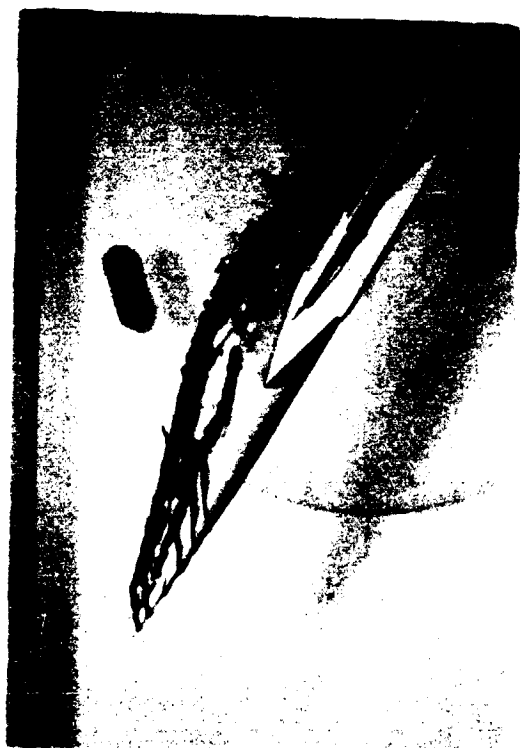


$\alpha = 40^\circ$



$\alpha = 50^\circ$

FIGURE 31. Cambered Forebody Flow Field; $(\dot{m}_1/\dot{m}_\infty)$ $\alpha = 0^\circ, \delta_{II} = -29^\circ, \delta_I = 11^\circ, \beta = 0^\circ$



$\alpha = 30^\circ$



$\alpha = 30^\circ$



$\alpha = 45^\circ$



$\alpha = 45^\circ$

FIGURE 32. Cambered Forebody Flow Field; $(\dot{m}_1/\dot{m}_2, \alpha = 0^\circ, \delta_{II} = -29^\circ, \delta_I = 11^\circ, \beta = 5^\circ)$



$\alpha = 35^\circ$



$\alpha = 50^\circ$



$\alpha = 35^\circ$



$\alpha = 50^\circ$

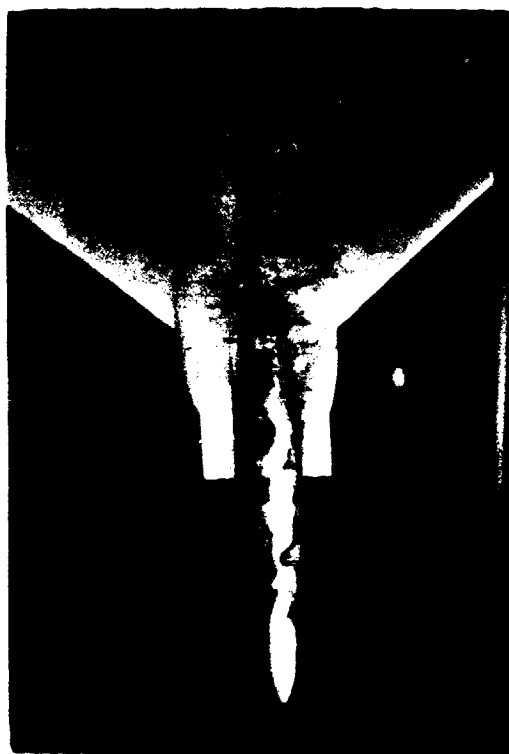
FIGURE 33. Effect of Nose Boom on Production Forebody; (\dot{m}_1/\dot{m}_2), $\alpha = 0^\circ$,
 $\delta_{II} = -29^\circ$, $\delta_I = 11^\circ$, $\beta = 0^\circ$



$\alpha = 35^\circ$



$\alpha = 50^\circ$



$\alpha = 35^\circ$



$\alpha = 50^\circ$

FIGURE 3.1. Effect of Nose Boom on Production Forebody; (\dot{m}_I/\dot{m}_∞), $\alpha = 0^\circ$, $\delta_{II} = -29^\circ$, $\delta_I = 11^\circ$, $\beta = 5^\circ$

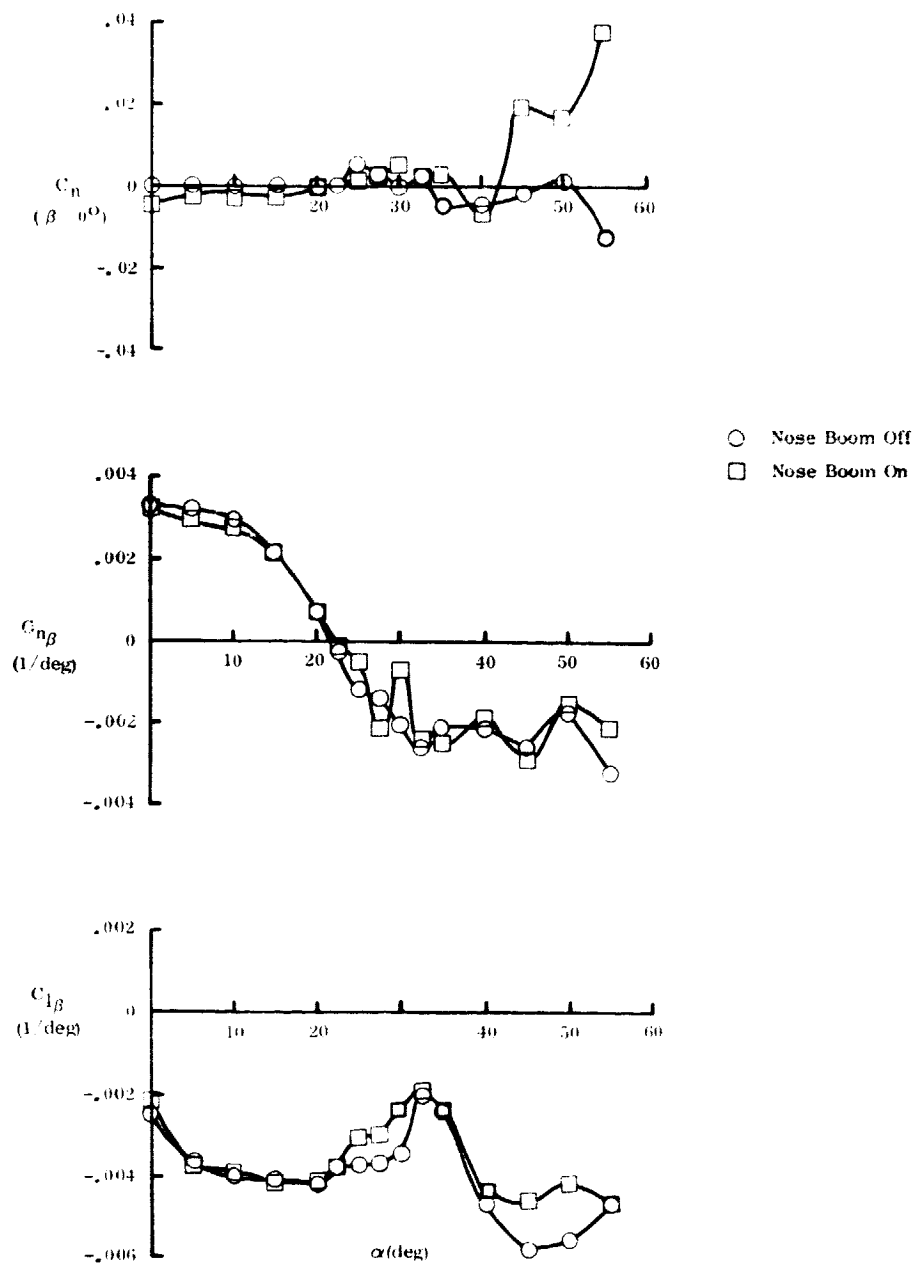
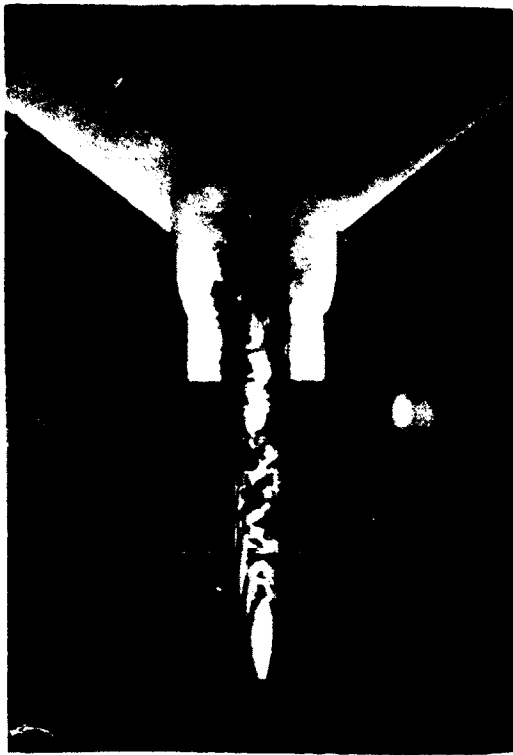


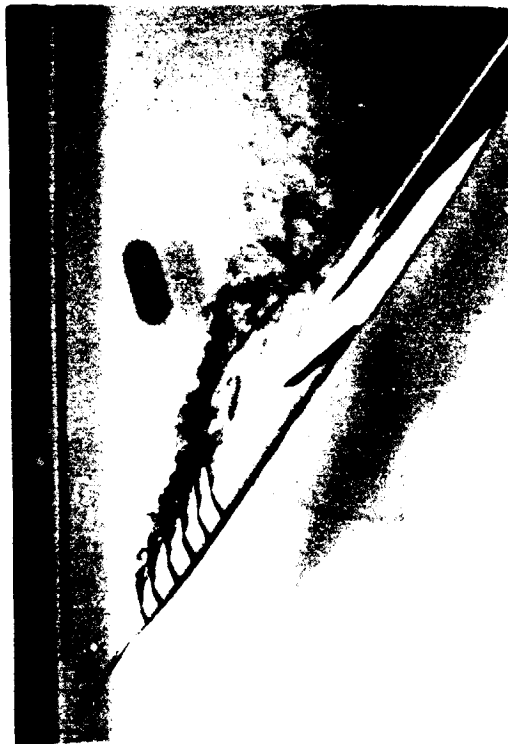
FIGURE 35. Effect of Nose Boom on Production Forebody; $\delta_{II} = 0^\circ$, $\delta_I = 12^\circ$



$\alpha = 35^\circ$



$\alpha = 50^\circ$



$\alpha = 35^\circ$



$\alpha = 50^\circ$

FIGURE 36. Effect of Nose Boom on Long Forebody; $(\dot{m}_1 / \dot{m}_\infty) \alpha = 0$,
 $\delta_{II} = -29^\circ$, $\delta_I = 11^\circ$, $\beta = 0^\circ$



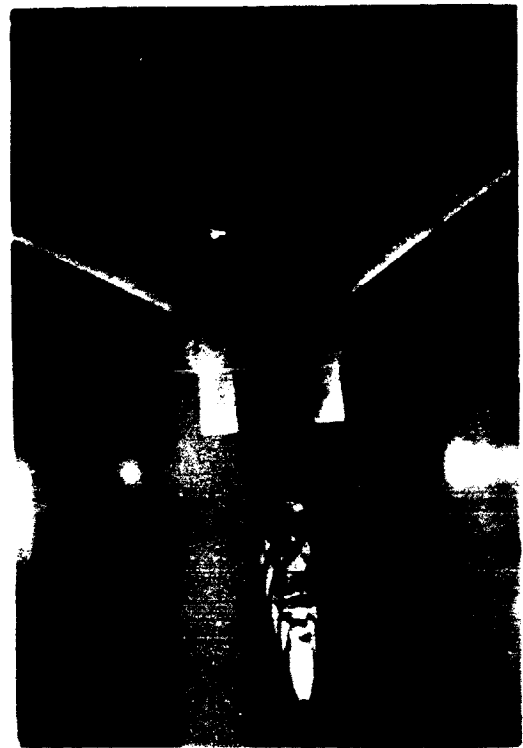
$\alpha = 30^\circ$



$\alpha = 30^\circ$



$\alpha = 50^\circ$



$\alpha = 50^\circ$

FIGURE 37. Effect of Nose Boom on Long Forebody; $(\dot{m}_I / \dot{m}_\infty)_{\alpha=0} = 0$,
 $\delta_{II} = -29^\circ$, $\delta_I = 11^\circ$, $\beta = 5^\circ$

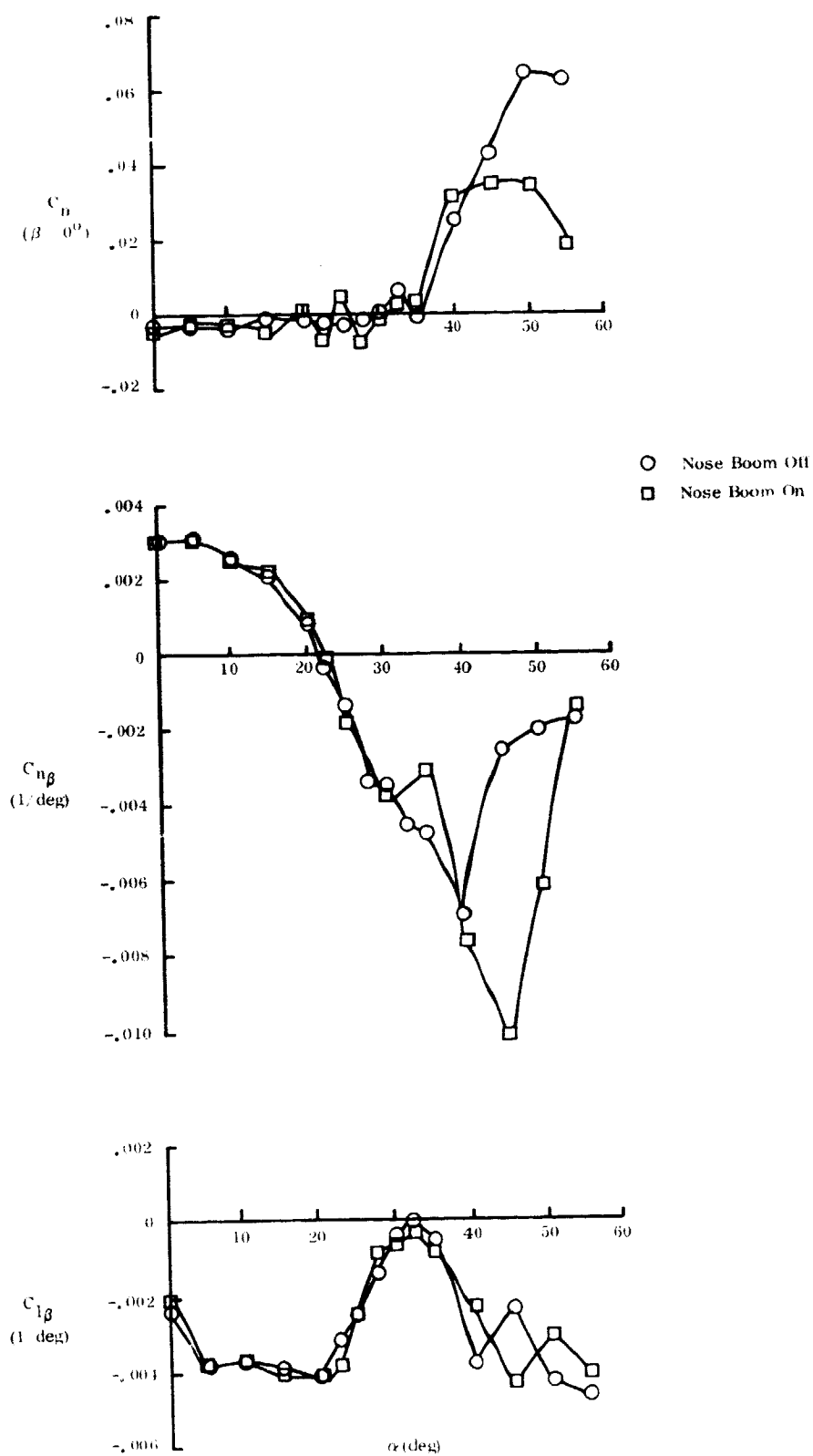
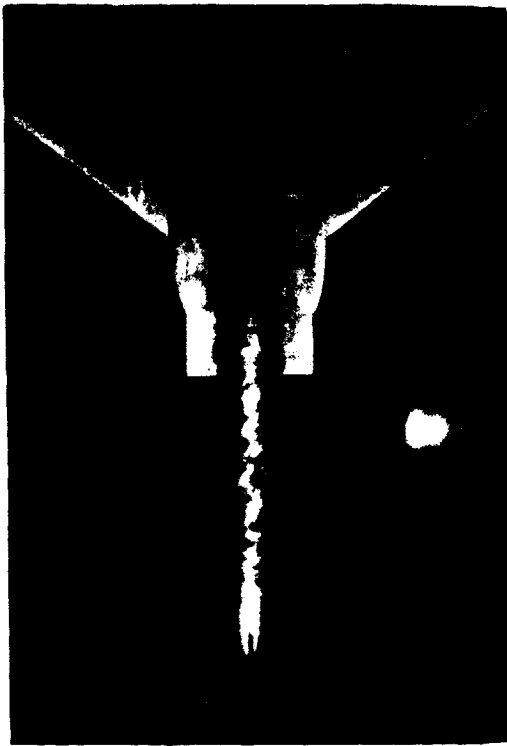


FIGURE 38. Effect of Nose Boom on Long Forebody; $\delta_H = 0^\circ$, $\delta_I = 12^\circ$



$\alpha = 35^\circ$



$\alpha = 50^\circ$



$\alpha = 35^\circ$

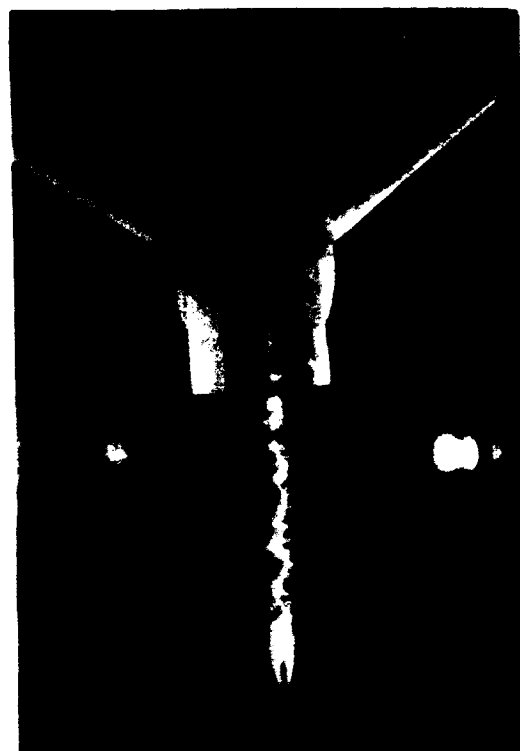


$\alpha = 50^\circ$

FIGURE 3.9. Effect of Nose Boom on Cambered Forebody; $(\dot{m}_I / \dot{m}_\infty) \alpha = 0, \delta_{II} = 0, \delta_I = -29^\circ, \beta = 11^\circ, \beta = 0^\circ$



$\alpha \ 40^\circ$



$\alpha \ 40^\circ$



$\alpha \ 50^\circ$



$\alpha \ 50^\circ$

FIGURE 40. Effect of Nose Boom on Cambered Forebody; $(\dot{m}_I/\dot{m}_\infty)\alpha \ 0, \delta_H \ 0, \delta_I \ -29^\circ, \delta_I \ 11^\circ, \beta \ 5^\circ$

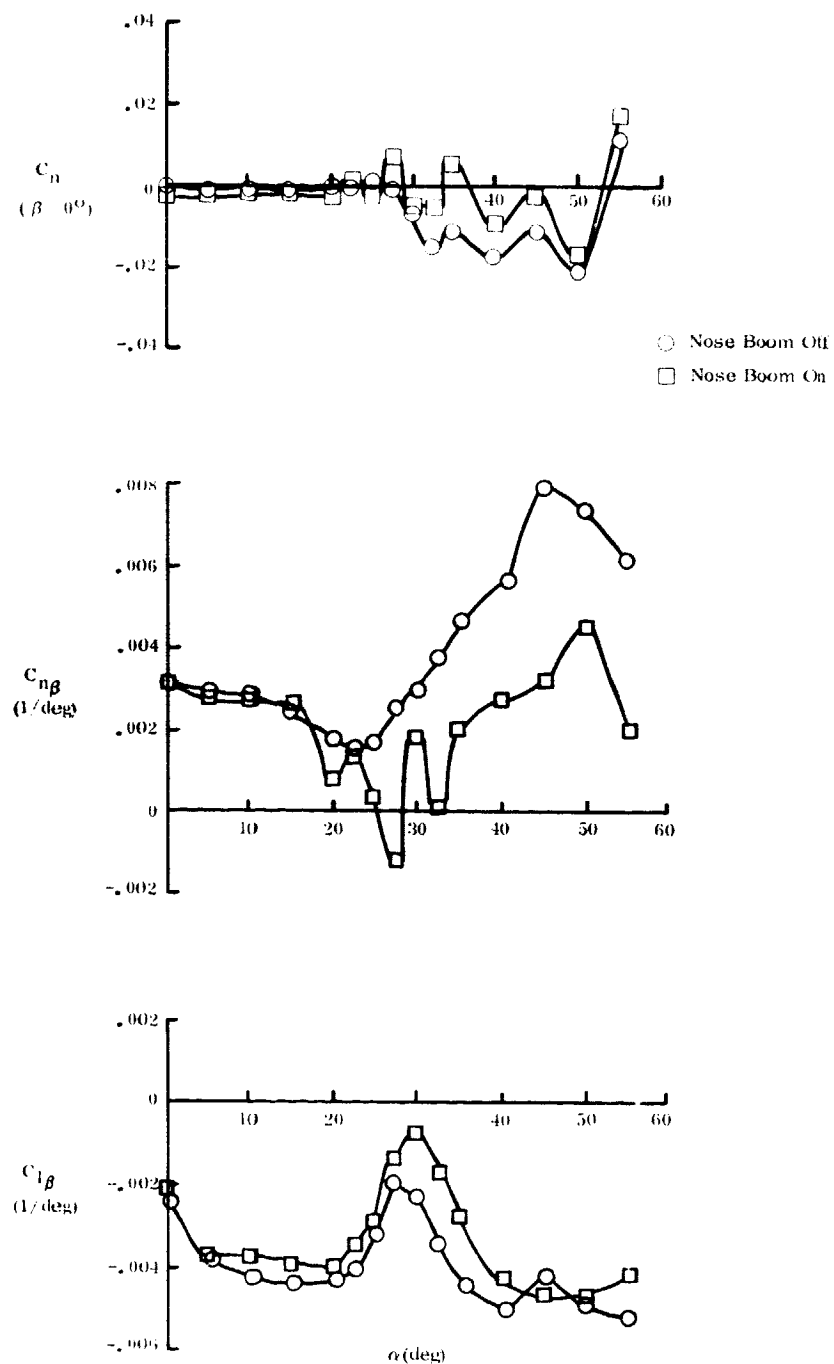


FIGURE 41: Effect of Nose Boom on Cambered Forebody; $\delta_H = 0^\circ$, $\delta_I = 12^\circ$

ORIGINAL PAGE IS
OF POOR QUALITY



$\alpha \ 35^\circ$



$\alpha \ 50^\circ$



$\alpha \ 35^\circ$

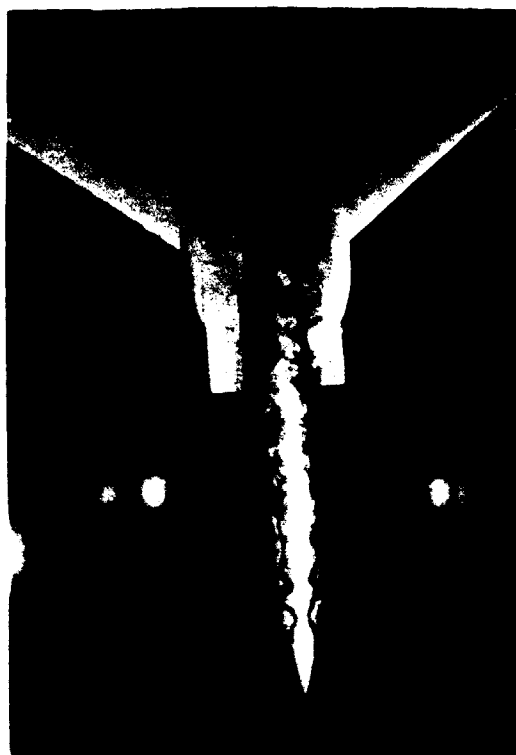


$\alpha \ 50^\circ$

FIGURE 4.2. Effect of Helical Nose Trip on Long Forebody; $(\dot{m}_I/\dot{m}_\infty) \alpha \ 0, \delta_{II} \ -29^\circ, \delta_I \ 11^\circ, \beta \ 6^\circ$



$\alpha \ 35^\circ$



$\alpha \ 35^\circ$



$\alpha \ 50^\circ$



$\alpha \ 50^\circ$

FIGURE 43. Effect of Helical Nose Trip on Long Forebody; $(\dot{m}_I/\dot{m}_\infty)\alpha \ 0$, $\delta_H \ -29^\circ$, $\delta_I \ 11^\circ$, $\beta \ 5^\circ$

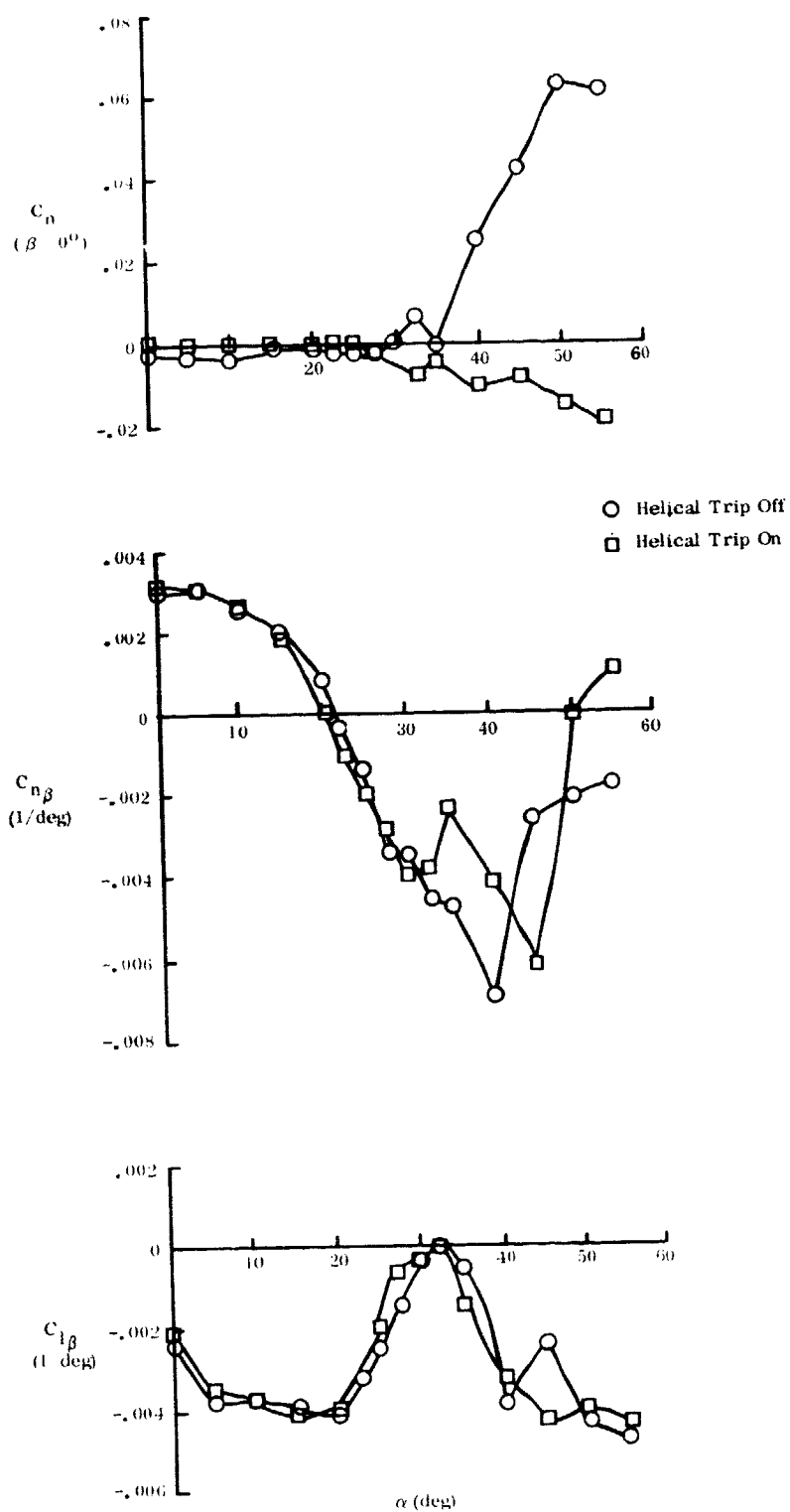
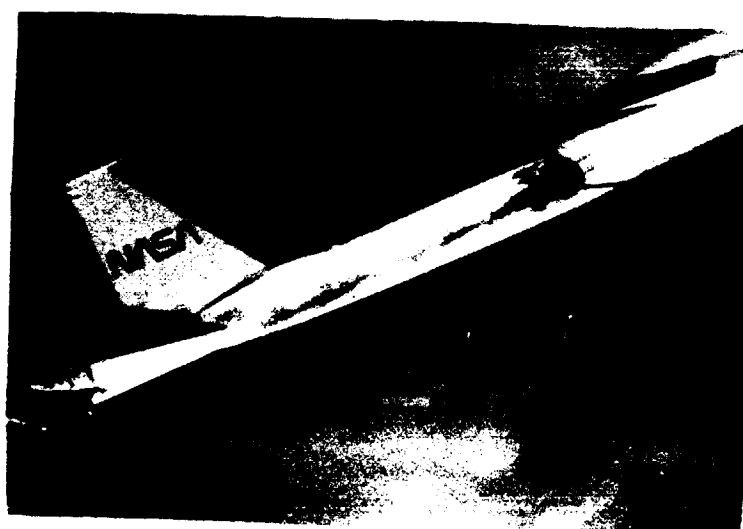


FIGURE 44. Effect of Helical Trip on Long Forebody; $\delta_H = 0^\circ$, $\delta_I = 12^\circ$

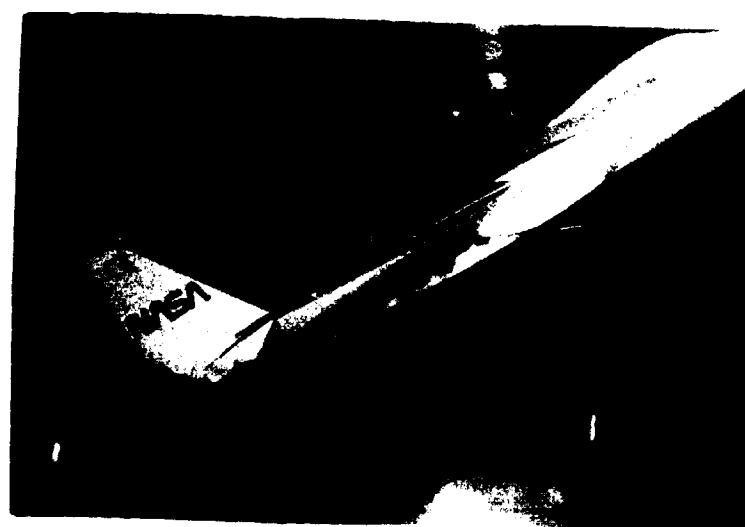
ORIGINAL PAGE IS
OF POOR QUALITY



$$\alpha = 10^\circ, \delta_H = -3.5^\circ$$

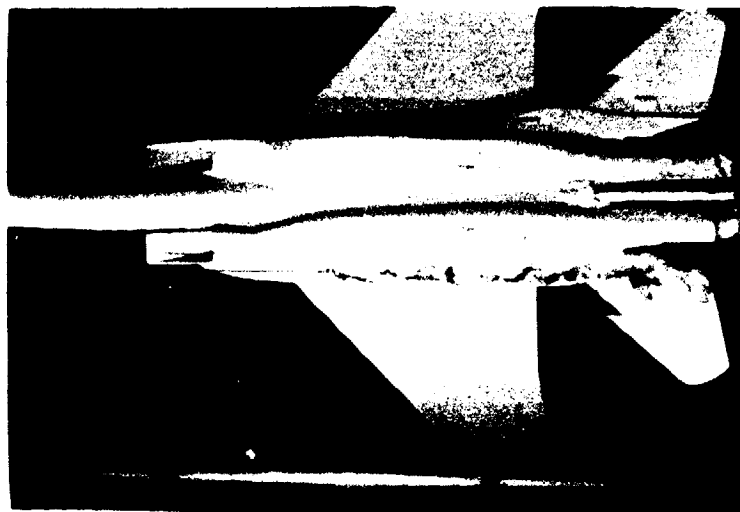


$$\alpha = 20^\circ, \delta_H = -10.5^\circ$$



$$\alpha = 30^\circ, \delta_H = -29^\circ$$

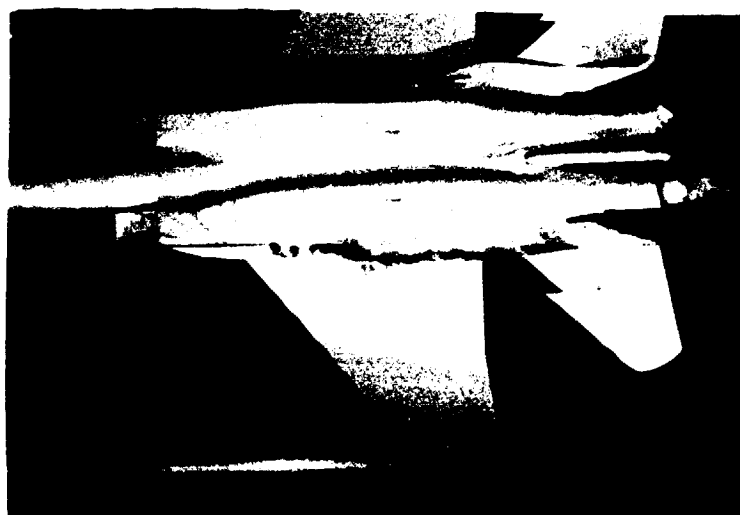
FIGURE 45. Wing-Fuselage Underside Vortex; $(\dot{m}_1 / \dot{m}_\infty)_{\alpha=0} = 1.85, \delta_1 = 0^\circ, \beta = 0^\circ$



$$\alpha = 10^{\circ}, \delta_{\text{II}} = -3.5^{\circ}$$



$$\alpha = 20^{\circ}, \delta_{\text{II}} = -10.5^{\circ}$$



$$\alpha = 30^{\circ}, \delta_{\text{II}} = -29^{\circ}$$

FIGURE 45. Concluded

**END
DATE
FILMED**

APR 24 1979